FOI-R--0720--SE
November 2002
ISSN 1650-1942
Technical report

Håkan Hansson, Peter Skoglund

Simulation of Concrete Penetration in 2D and 3D with the RHT Material Model

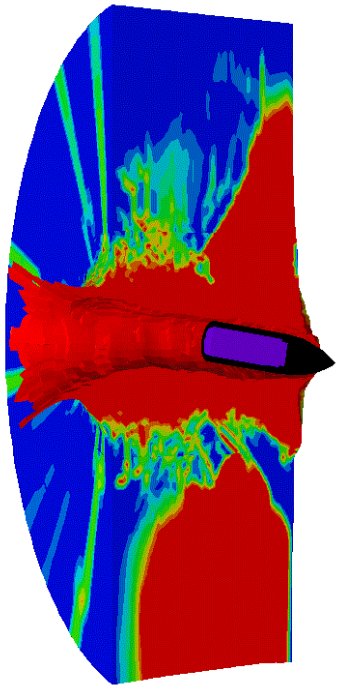

Weapons and Protection
SE-147 25 Tumba

SWEDISH DEFENCE RESEARCH AGENCY
Weapons and Protection
SE-147 25 Tumba

FOI-R--0720--SE
November 2002
ISSN 1650-1942
Technical report

Håkan Hansson, Peter Skoglund

Simulation of Concrete Penetration in 2D and 3D with the RHT Material Model

Issuing organization	Report number, ISRN	Report type
FOI – Swedish Defence Research Agency Weapons and Protection SE-147 25 Tumba	FOI-R--0720--SE	Technical report
	Research area code 5. Combat	
	Month year November 2002	**Project no.** E2011
	Customers code 5. Commissioned Research	
	Sub area code 53 Protection and Fortification	

Author/s (editor/s)	Project manager
Håkan Hansson Peter Skoglund	Johan Magnusson
	Approved by
	Sponsoring agency Swedish defence HQ
	Scientifically and technically responsible

Report title

Simulation of Concrete Penetration in 2D and 3D with the RHT Material Model

Abstract (not more than 200 words)

In this report results from numerical simulations of a steel projectile penetrating a concrete target are discussed. The simulations are performed with the Autodyn software in 2D and 3D, and the mechanical properties of the concrete are described with the RHT model. This advanced material model incorporates elastic limit, failure and also residual strength of the crushed concrete under pressure. As a consequence, the RHT model contains a large number of constants. In this report, a study of the relative importance in 2D- and 3D simulations of some of the parameters on the penetration is performed. An advantage with 3D simulations is that more realistic penetration cases with oblique impact can be done. However, 3D simulations lead to a large number of elements and thus also to long calculation times. Therefore a parallel processor system has been tested. The numerical results are, when possible, compared to experimental ballistic tests done in 1999.

The study shows that the RHT constants describing damage evolution and residual strength of the concrete are very important for penetration calculations. Another important finding is that the impact geometry must be well defined, since even a very small deviation from normal impact results in a large effect on the calculated penetration path.

Keywords

Numerical simulation, Concrete penetration, RHT model

Further bibliographic information	Language English
ISSN 1650-1942	**Pages** 49 p.
	Price acc. to pricelist

Utgivare	Rapportnummer, ISRN	Klassificering
Totalförsvarets Forskningsinstitut - FOI	FOI-R--0720--SE	Teknisk rapport
Vapen och skydd 147 25 Tumba	**Forskningsområde** 5. Bekämpning	
	Månad, år November 2002	**Projektnummer** E2011
	Verksamhetsgren 5. Uppdragsfinansierad verksamhet	
	Delområde 53 Skydd och anläggningsteknik	

Författare/redaktör	Projektledare
Håkan Hansson Peter Skoglund	Johan Magnusson
	Godkänd av
	Uppdragsgivare/kundbeteckning Försvarsmaktens högkvarter
	Tekniskt och/eller vetenskapligt ansvarig

Rapportens titel (i översättning)

Simulering av betongpenetration i 2D och 3D med RHT modellen

Sammanfattning (högst 200 ord)

I denna rapport redovisas resultaten från numeriska simuleringar av en stålprojektils penetration i betong. Simuleringarna är gjorda med programmet Autodyn i 2D och 3D, där betongmålets mekaniska egenskaper modelleras med RHT-modellen. Denna avancerade modell beaktar elastiska gränsen, brottgränsen och resthållfastheten hos det skadade materialet under tryck. Modellen innehåller således en stor mängd material-konstanter som är svåra att bestämma experimentellt. Ett syfte med denna rapport är att göra en studie av några av de ingående konstanterna för att bestämma deras betydelse för penetrationsberäkningar i 2D och 3D. En fördel med 3D simuleringar är att beräkningar av realistiska fall med olika typer av snedställda projektiler kan göras. Dessa simuleringar leder dock till ett stort antal element och därmed lång beräkningstid. För att motverka detta har ett parallellprocessorsystem prövats. De numeriska simuleringsresultaten jämförs där så är möjligt med experimentella ballistiska försök utförda 1999.

Studien visade att beskrivningen av skadeutvecklingen och resthållfastheten är mycket viktiga. Vidare framgår att projektilens anslagsgeometri måste vara väl bestämd eftersom även en mycket liten avvikelse från vinkelrätt anslag leder till stora skillnader i simulerat penetrationsbeteende.

Nyckelord

Numerisk simulering, Betongpenetration, RHT modellen

Övriga bibliografiska uppgifter	Språk Engelska
ISSN 1650-1942	**Antal sidor:** 49 s.
Distribution enligt missiv	**Pris: Enligt prislista**

This page is intentionally blank

CONTENTS

CONTENTS 5
1. Introduction 6
2. Material modelling 7
2.1. Material models for the steel 7
2.1.1. Equation of state for the steel 7
2.1.2. Strength model for the steel 8
2.2. Material models for the concrete 9
2.2.1. Equation of state for the concrete 9
2.2.2. Strength model for the concrete 10
3. Simulation of penetration tests 14
3.1. Material parameters for the concrete target 15
3.2. Problem geometry 18
3.3. 2D penetration simulations 19
3.3.1. 2D simulations with Lagrange target formulation 19
3.3.2. 2D simulations with SPH target formulation 23
3.3.3. Conclusions considering 2D simulations 25
3.4. 3D penetration simulations 26
3.4.1. 3D simulations with Lagrange target formulation 26
3.4.2. 3D simulations with ALE target formulation 29
3.4.3. 3D simulations with Lagrange target formulation and non-normal impact 29
3.4.4. Conclusions considering 3D simulations 32
3.4.5. Parallel 3D simulations 32
4. Discussion 34
5. Future research 35
References 36
Appendix 1: Equations and parameters 37
Appendix 2: Benchmark tests 40

1. INTRODUCTION

Today the investigation of highly dynamic events like projectile penetration or loading by blast waves is supported by numerical calculations. These calculations are usually performed with wave propagation codes or hydrocodes which solve the conservation equations for mass, momentum and energy. In addition, models that describe the mechanical response of the materials when subjected to external loads are needed. Such constitutive equations for concrete exposed to weapons effects have been a major area of interest for a long time, and several material models for concrete are developed. However, it is not until recent years with the development of both advanced concrete models and new numerical solution methods that it seems possible to model the behaviour of concrete targets during projectile penetration with acceptable results.

In this report, an advanced material model for concrete is described and used in simulations of steel projectiles penetrating into concrete targets. This RHT concrete model was developed by, and named after Riedel, Hiermaier and Thoma, see Riedel et. al. (1998, 1999, 2000). The version of the material model used is implemented as a standard model in the commercial hydrocode software Autodyn version 4.2 or higher. With the latest development in material and numerical modelling it is possible to use such advanced material models together with alternative element formulations. In the work reported here a parametric study of the influence of some different RHT parameters on the simulated projectile penetration into concrete is done. The simulations are performed with several different element formulations of the concrete target as described later. Included in the investigation are, apart from two dimensional (2D) simulations, also tests using the three dimensional (3D) version of the software. This is a major enhancement of the possibility to model more realistic non-symmetric ballistic impact events, for example projectiles with pitch and yaw. The results using both the 2D and 3D implementations with different element formulations are discussed and compared. When possible, the ballistic benchmark test series from 1999 with 152 mm ogive nosed projectiles impacting on concrete are used as a reference case for the simulations.

The computational time for the 3D simulations are much longer than the corresponding 2D calculations due to the large increase of elements in the 3D grid. However, the 3D software supports calculations using parallel processors and the development of such systems has increased the possibility to obtain computer capacity for advanced simulations at a reasonable expense. These parallel computations are performed with standard personal computers connected through a local area network and running Windows 2000 or Linux. This reduces the computational cost considerably compared to high level Unix workstations and gives the opportunity for demanding computer simulations at a reasonable cost. Thus, a minor investigation using a parallel processor system consisting of 2 and 4 processors has been tested and compared to single processor calculations.

2. MATERIAL MODELLING

To solve a dynamic material problem it is necessary to utilise the conservation laws of mass, momentum and energy together with appropriate initial and boundary conditions. A complete solution also demands a material model which relates stress to deformation and energy. In hydrocodes, such as Autodyn, this is usually done by separating the total stress tensor into a hydrostatic pressure and a deviatoric stress. The hydrostatic pressure is uniform with all three normal stresses equal and is related to the density (specific volume) and energy (or temperature) by an equation of state (EOS). On the other hand, the deviatoric stress tensor describes the material's resistance to shear distortion using a strength model. Thus, the EOS and the strength model gives the volumetric and the distortional changes of a material subjected to load respectively.

Depending on the type of material and the characteristics of the loads in the problem, different types of EOS and strength models are used. In this case with a steel projectile penetrating a concrete target the projectile is described with a "shock" equation of state together with a strength equation suggested by Johnson and Cook. The concrete target is modelled by a "P-α" EOS and a strength model developed by Riedel, Hiermaier and Thoma.

Finally, a criteria for failure of the material is also needed and in the following the chosen material models are discussed and described.

2.1. Material models for the steel

In the specific case of a steel projectile penetrating a concrete target, the strength of the projectile is much larger than the strength of the concrete and usually no deformation, apart from minor surface erosion, is found on the projectile after impact. Despite this, an equation of state and a strength model for the projectile material are needed in order to calculate the stresses and wave phenomena that develop in the penetrator during impact. In Autodyn numerous different forms of EOS and strength models are incorporated which are suitable for different applications. In the following the shock EOS and the Johnson and Cook strength equation used for the projectile are briefly discussed. A more thoroughly description is given by for example Meyer.

2.1.1. Equation of state for the steel

The equation of state for the steel projectile is given by a shock equation of state, where the pressure P as a function of density (specific volume V) and specific internal energy e is described by a Mie-Grüneisen equation.

$$P = P_H + \frac{\gamma}{V}(e - e_H) \tag{1}$$

The reference states P_H and e_H are set to the Hugoniot-shock curve and γ is the Grüneisen constant $\left(\frac{dp}{de}\right)_V$.

Thus, the pressure and internal energy on a point off the Hugoniot is related to the pressure and internal energy on the Hugoniot at the same volume. Further, as seen, in the Mie-Grüneisen form the pressure varies linearly with internal energy at constant volume. The input data for the Mie-Grüneisen EOS is usually given as a linear relationship between the shock velocity (U_s) and the particle velocity (U_p), which can be related to other necessary parameters, see for example Meyer. The empirical equation for the "shock" equation of state used for the projectile is found below, with the notation used by Autodyn.

$$U_s = C_1 + S_1 U_p \tag{2}$$

With C_1 being the sound velocity at zero pressure and S_1 is the slope in a plot of shock velocity versus particle velocity. Table 2.1 presents the necessary material data for the shock equation of state for the projectile.

2.1.2. Strength model for the steel

The Johnson and Cook (1983) material model describes the relation between the flow stress σ of a metal and the strain ε, strain rate $\dot{\varepsilon}$ and temperature T. The Johnson and Cook equation has successfully been used to describe the constitutive behaviour of a number of metals and is very often used for penetration simulation. Even if the projectile behaves more or less as a rigid body, it is suitable to use a deformable projectile for the simulations. The reason is to get feedback on the projectile behaviour and limit the stresses in the projectile. This ensures that the pressure in the target does not reach levels that will damage the projectile.

$$\sigma = \left(A + B\varepsilon^n\right)\left(1 + C\ln\frac{\dot{\varepsilon}}{\dot{\varepsilon}_0}\right)\left(1 - \left(\frac{T - T_r}{T - T_m}\right)^m\right) \tag{3}$$

In this equation, T_r and $\dot{\varepsilon}_0$ is a reference temperature (room temperature) and reference strain rate (1 s^{-1}) at which the material parameters A (Pa), B (Pa) and n are determined. The constant C in the second term takes the strain rate dependency into account. Finally, in the third term, T_m is the melting temperature and m is a parameter that includes the effect of temperature on the flow stress. It is emphasised that the model is semi-empirical and that influence of strain hardening (first term), strain rate (second term) and temperature (third term) are decoupled from each other. Material parameters for the projectile are shown in table 2.1. Since the main purpose of this report is to study the RHT model parameters and its implementation in the Autodyn software the material data for the projectile is given here only.

Table 2.1. Equation of state and strength model for the projectile (Steel S7).

Shock equation of state			Johnson & Cook strength model	
Reference density (g/cm^3)	7.75		Bulk modulus (GPa)	159
Grüneisen coefficient, γ	2.17		Shear modulus (GPa)	81.8
Parameter C_1 (m/s)	4,569		Yield stress, A (MPa)	1539
Parameter S_1 (m/s)	1.49		Hardening constant, B (MPa)	477
Reference temperature (K)	300		Hardening exponent, n	0.18
Specific heat (J/kgK)	477		Strain rate constant, C	0.012
			Thermal softening exponent, m	1.0
			Melting temperature, T_m (K)	1763

2.2. Material models for the concrete

Concrete is a very complex composite material with aggregates, varying in size, embedded in a matrix of porous grout. Thus, due to the inherent inhomogenity it is difficult to describe the mechanical behaviour of the concrete. However, Herrman (1969) has developed a general equation of state that takes porosity into account and this has been incorporated as an important part of the concrete EOS discussed briefly below. The RHT strength model also includes residual strength of the failed material under compression. The main components of the material models are given here, while a detailed description are given by Herrman (1969) and Riedel et al. (1998, 1999, 2000).

2.2.1. Equation of state for the concrete

Concrete has a complex non-linear compression behaviour due to the inhomogenity and the porosity of the material. Herrman has proposed a porous equation of state that takes this into account. The equations below describe the most essential part of Herrman's model, and the entire parameter list used for the concrete EOS can be seen in table A2 in the appendix, together with a short explanation. The behaviour of the fully compacted material is, in this case, described with a polynomial according to equation 4, while the porous material is scaled using the porosity α with respect to the fully compacted material as the reference. Thus, for the fully compacted material the pressure P equals P_{lock} and the porosity α is 1 and the pressure is calculated using equation 4. For pressures between the initial pore crush pressure P_{crush} and P_{lock} the pressure is scaled with equation 5. The compaction, $\alpha(P,e)$, gives the behaviour of the porous material in the pressure range of pore collapse (P_{crush}) and full compaction (P_{lock}). A more thorough description can be found in the report by Riedel (1998).

$$P = A_1\mu + A_2\mu^2 + A_3\mu^3 + (B_0 + B_1\mu)\rho_0 e \quad with \quad \mu = \frac{\rho}{\rho_0} - 1 \tag{4}$$

$$P = f(\rho, e) \quad \overset{porous}{\rightarrow} \quad P = f(\rho\alpha, e) \quad with \quad \alpha = 1 + (\alpha_{init} - 1)\left[\frac{P_{lock} - P}{P_{lock} - P_{crush}}\right]^n \tag{5}$$

As mentioned, there are additional parameters required for a complete EOS and in table 3.2 the constants used in the numerical simulations are tabulated. For convenience all concrete material parameters also are listed in appendix 1.

2.2.2. Strength model for the concrete

Concrete, like many other hard and brittle materials, is sensitive to tensile loading and fractures at small deformations. On the other hand, with increasing pressure the strength of the concrete also increases. Further, in case of confinement the flow resistance of the crushed concrete under compression can be very significant. The different tensile and compressive behaviour of the concrete under deformation together with the residual strength of the material under compression indicates that a complex strength model is needed. Thus, models for hydrocodes which include all these phenomenon are rare. However, Riedel, Hiermaier and Thoma have suggested a model (RHT) that has shown promising results for prediction of penetration depths in concrete targets. The model is currently implemented in Autodyn 2D and 3D and this report describes, in general terms, the RHT concrete model. The first version of the RHT concrete model is presented in Riedel (1998), together with examples of material parameters for concrete. A thoroughly description is also presented in the dissertation thesis by Riedel (2000). The RHT concrete strength model has been used in several simulation approaches using Autodyn 2D, see for example Riedel et. al. (1999), Hansson et. al. (2000, 2001), Ågårdh and Hansson (1999) and Svinsås with co-workers (2001). The 2D and 3D simulations in this report are performed with the RHT model as implemented in Autodyn version 4.2.03 and described briefly in the following.

The descriptions of the stress state in the material model is based on the three invariants of the stress tensor for the definition of the elastic limit surface, failure surface and remaining residual strength surface for the crushed material, see figure 2.1. These three surfaces all are pressure dependent and described below. The failure surface can be seen as a function of the strength along the compression meridian $Y_{TXC}(P)$ multiplied by the factors $F_{Rate}(\dot{\varepsilon})$ and $R_3(\theta)$ as in equation 6.

$$Y_{fail}(P,\theta,\dot{\varepsilon}) = Y_{TXC}(P)F_{Rate}(\dot{\varepsilon})R_3(\theta) \tag{6}$$

The strength along the meridian is given by equation 7, where $Y^*_{TXC}(P)$ defines the pressure dependent curved meridian of three axial compression normalised to the unconfined compression strength f_c. Further, P^* and P^*_{spall} are the pressure and spall strength respectively divided by f_c, while A and N are material constants characteristic for the specific concrete investigated.

$$Y^*_{TXC}(P) = \frac{Y_{TXC}(P)}{f_c} = A \cdot \left[P^* - \left(P^*_{spall}F_{Rate}\right)\right]^N \tag{7}$$

The factor $F_{RATE}(\dot{\varepsilon})$ takes the strain rate enhancement into account and follows from equation 8 below.

$$F_{RATE}(\dot{\varepsilon}) = \begin{cases} \left(\dfrac{\dot{\varepsilon}}{\dot{\varepsilon}_0}\right)^{\alpha} & for\ P > f_c/3\ ,\ with\ \dot{\varepsilon}_0 = 30\times10^{-6}\ s^{-1} \\ \left(\dfrac{\dot{\varepsilon}}{\dot{\varepsilon}_0}\right)^{\delta} & for\ P < f_c/3\ ,\ with\ \dot{\varepsilon}_0 = 3\times10^{-6}\ s^{-1} \end{cases} \tag{8}$$

As seen different strain rate enhancements are used in different pressure regions, with α and δ being material constants.

Reduced failure strength for states off the compression meridian on the failure surface is introduced and given by a factor $R_3(\theta)$. The factor, which scales the strength from the highest value at the compression meridian, is given by equation 9. Thus, with θ rotating around the hydrostatic axis the entire failure surface can be calculated, see also figure 2.1.

$$R_3(\theta) = \frac{2\left(1-Q_2^2\right)\cos\theta + \left(2Q_2-1\right)\left[4\left(1-Q_2^2\right)\cos^2\theta + 5Q_2^2 - 4Q_2\right]^{\frac{1}{2}}}{4\left(1-Q_2^2\right)\cos^2\theta + \left(1-2Q_2\right)^2} \tag{9}$$

The strength reduction as described by $R_3(\theta)$ depends also of Q_2. This parameter is the distance from the hydrostatic axis to the tensile meridian divided with the distance between the hydrostatic axis to the compressive meridian. The extreme case of Q_2 = 0.5 is found at low tensile pressures giving a triangular failure surface with rounded corners in the deviatoric plane. At the other extreme, Q_2 = 1, gives a circular cut on the deviatoric plane. Thus at large confining pressures the surface approaches the circular form. The pressure dependence of Q_2 follows from equation 10. This method to account for reduced concrete strength off the compression meridian was first used by William and Warnke (1975).

$$Q_2 = Q_{2,o} + BQ \cdot P^* \; with \; 0.51 \le Q_2 \le 1 \; and \; BQ = 0.0105 \tag{10}$$

The elastic limiting surface is scaled around P=0 and σ_{eq}=0 from the failure surface and the scaling factors varies linearly, depending on the pressure, according to TENSRAT and COMPRAT. Where COMPRAT defines the ratio between the elastic compressive limit and the compressive strength and TENSRAT the corresponding ratio in tension. The slope of the elastic-plastic part is given by PREFACT, which defines the ratio between the original shear modulus and the corresponding value after the elastic limit has been passed. The elastic part of the deformation decreases at high pressures and the option to use a "cap" on the elastic surface ensures that the elastic surface closes at high pressures. Thus, by multiplying the right part of equation 6 above with a dimensionless factor $F_{CAP}(P)$, which goes smoothly from unity to zero, the elastic surface can be forced to close at high pressures. The cap function is unity up to the pressure P_u where the uniaxial compression path intercepts with the elastic surface. At higher pressures $F_{CAP}(P)$ decreases and reaches zero at the pressure $P_o = f_c/3$, which is close to the pore crush pressure. In equation 11 below the mathematical expression for $F_{cap}(P)$ is given.

$$F_{CAP}(P) = \begin{cases} 1 \quad for \; P \le P_u \\ \sqrt{1-\left(\dfrac{P-P_u}{P_o-P_u}\right)^2} \; for \; P_u < P < P_0 \\ 0 \; for \; P_0 \le P \end{cases} \tag{11}$$

The damage in the material grows after the stress point passes the failure surface according to equations 12 and 13. Where the accumulated plastic strain $\Delta\varepsilon_p$ is compared to the failure strain $\varepsilon_p^{failure}$ which is pressure dependent and given by equation 13 with the material parameters D_1

and D_2. At low pressures, a lower limit of the failure strain is set by introducing $E_{f,min}$ as also seen in figure 3.3. The strain measures include here both volumetric and deviatoric contributions.

$$D = \sum \frac{\Delta \varepsilon_p}{\varepsilon_p^{failure}} \tag{12}$$

$$\varepsilon_p^{failure} = D_1 \left(P* - P*_{spall} \right)^{D_2} \tag{13}$$

The residual strength $Y^*_{residual}$ (normalised to the unconfined compression strength) of the fully damaged concrete is calculated from equation (14). The strength is then interpolated from the strength values for the undamaged material (D=0) at the failure surface and the completely damaged material (D=1) according to equation (15).

$$Y^*_{residual} = B \cdot \left(P^* \right)^M \tag{14}$$

$$Y^*_{fractured} = (1 - D) Y^*_{failure} + D \cdot Y^*_{residual} \tag{15}$$

In figure 2.1 some of the characteristics of the RHT model are schematically shown. An important difference compared to the Johnson and Cook strength model for the steel projectile is the pressure dependency of the strength. It is also important to note that, concrete under compression, has an additional strength surface for the failed material.

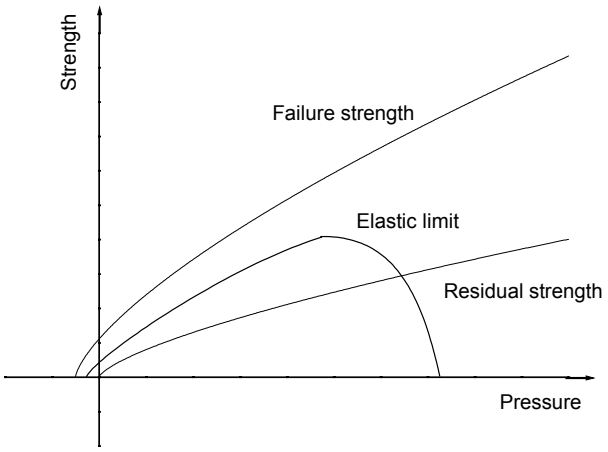

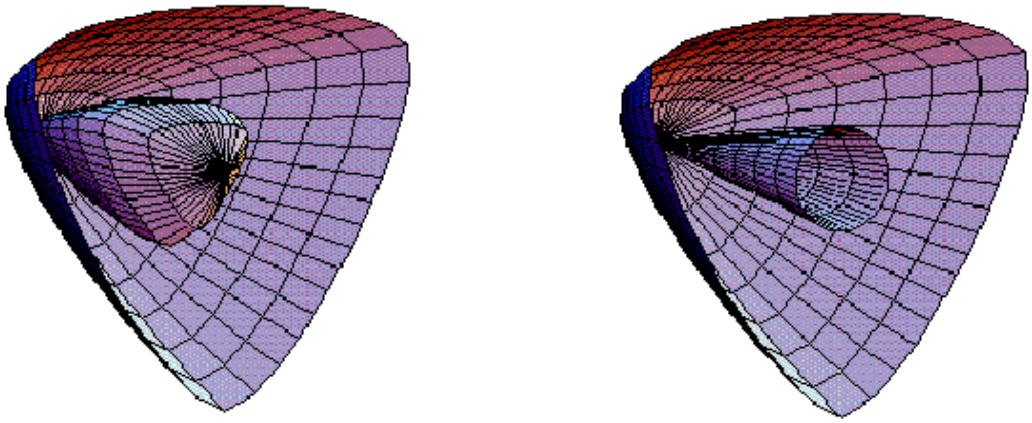

Figure 2.1. The top graph shows a 2D view of the three surfaces along the compression meridian. The figure left down show the failure surface (outer) and the elastic limit surface (inner), while the right give the failure surface (outer) and the residual strength surface (inner) as 3D-projections. After Riedel (1998).

As seen above, a large number of parameters are needed to give a full characterisation of the concrete. In chapter 3.1 the RHT parameters used for this specific concrete are given and the relative importance of some of the constants are investigated. For convenience, all concrete material data are compiled and given a short explanation in appendix 1, table A.1.3.

3. SIMULATION OF PENETRATION TESTS

In 1999 a series of benchmark tests with instrumented steel projectiles impacting on concrete targets were conducted at the Bofors test centre in Karlskoga. The tests were a cooperation project with DERA (Defence Evaluation and Research Agency) in the UK, FFI (Forsvarets forskningsinstitutt) in Norway, TNO (The Netherlands Organisation for Applied Scientific Research) from Holland and FOA Sweden as participants and one important aim was to obtain reliable data for numerical simulations. The result from the benchmark test is published before (Hansson 2001). For convenience the part of the report by Hansson describing the ballistic data and concrete material test procedures and properties are also given in appendix 2. As a short review, the test was done with steel projectiles with length 55 cm and diameter 15.2 cm impacting on concrete targets with diameter 240 cm and thickness 75 cm, see figure 3.1.

Figure 3.1. The steel projectile and the concrete target used for the benchmark tests in 1999, see also appendix 2. From Hansson 2001.

The main results from the benchmark test series are summarised in table 3.1 below. It is noted that the projectile velocity is reduced from about 460 m/s at impact to approximately 190 m/s at exit after perforation of the concrete target. After perforation, the steel projectile is more or less undeformed with only minor surface erosion. The mechanical properties of both concrete and projectile are further discussed by Hansson (2001) as presented in appendix 2.

Table 3.1. Benchmark test data.

	Test 23	Test 24	Test 25	Mean value
Diameter	152 mm			
Length	552 mm			
Ogive radius	380 mm			
Nose length	228 mm			
Total mass	46.2 ±0.1 kg			
Mass of case	38.8 kg			
Type of projectile	Dummy	Instrumented*	Instrumented	----
Impact velocity	460.0 ±0.5 m/s	455.5 ±0.2 m/s	458.8 ±0.2 m/s	458.1 ±0.2 m/s
Exit velocity**	183 ±6 m/s	204 ±4 m/s	181 ±4 m/s	190 ±14 m/s

**: Instrumentation pack not recovered after test.*
***: Determined from high speed video.*

A simulation of the experimental benchmark penetration tests described above is done as well as a minor number of calculations with a non-normal projectile impact. The numerical work incorporates hydrocode simulations using both 2D and 3D versions of the Autodyn software. The element formulations are Lagrange and SPH (Smooth Particle Hydrodynamics) for the 2D-simulations, while the 3D calculations are done with Lagrange and ALE (Arbitrary Lagrange Euler) grids for the concrete target in combination with the advanced RHT material model. The material models used to describe both the steel projectile and the concrete target are discussed in chapter 2. The main purpose is to investigate the sensitivity of some important RHT parameters on the projectile penetration. Knowledge on the relative importance of the parameters can act as a guide for future experimental work considering the determination of the material constants and developments of the model. Further, the 2D and 3D versions are compared and the new possibilities with 3D simulations are discussed. The 3D software allows the simulation of more realistic non-symmetric impact cases such as projectiles with yaw and pitch, and some initial results of different geometric impact cases are shown.

3.1. Material parameters for the concrete target

Considering the equation of state the pressure vs. density data is based on results from FFI shown in appendix 2 figure A.2.1. This ratio between pressure and density, is determined under static loading. However, it is known that the relationship between pressure and density is influenced by the loading rate for the material. It has been shown that a high strain rate results in greater pressure for the same compaction of the concrete. According to this it is difficult to determine a correct EOS to be used for the concrete subjected to high strain rate loading from static tests. However, no dynamic data are available and the static values are used. Parameters for the P-α model are given in table 3.2.

Table 3.2. P-α equation of state for concrete, based on the test performed by FFI.

Parameter	Value		Parameter	Value
ρ_0	2.39 g/cm^3		A_1	40 GPa
ρ_{porous}	2.39 g/cm^3		A_2	0 GPa
C_{porous}	3000 m/s		A_3	0 GPa
p_{crush}	80 MPa		B_0	1.22
p_{lock}	1800 MPa		B_1	1.22
n	5		T_1	40 GPa
Solid EOS	Polynomial		T_2	0 GPa
ρ_{solid}	2.54 g/cm^3		T_{ref}	300 K
			C_v	640 J/kgK

Compared to equations 4 and 5 the additional parameters (T_1 and T_2) in table 3.2 corresponds to the polynomial equation of state in tension, while the $A_{1\text{-}3}$ are the compression EOS data. The heat capacity C_v is used for temperature (energy) calculations and the porous sound speed C_{porous} is related to the shock wave velocity in a similar manner as in equation 2, see also Meyer.

Turning to the strength model, the chosen values of the material parameters for the RHT description are partly based on the material tests described in the previous chapter. However, some parameters are taken from literature while some are approximated from experience of the behaviour of other concrete materials as discussed below.

The unconfined compressive strength f_c is 92 MPa taken from uniaxial cylinder compression experiments. The uniaxial tensile strength f_t is normally 80% to 90% of the splitting strength. Therefore, f_t was chosen as 5.2 MPa, which is approximately 80% of the splitting strength for 150 mm cubes and 90% of the splitting strength for ∅100 mm cylinders, see also table A.2.1 in the appendix. As discussed before, the constant *COMPRAT* defines the ratio between the compressive elastic limit and the compressive failure strength and *TENSRAT* the corresponding ratio in tension. Based on stress-strain data from uniaxial tests *COMPRAT* was assumed to be 0.75. Further, the constant TENSRAT was chosen to 0.8 since it is known that this ratio is larger than COMPRAT. Moreover, the ratio between elastic and elastic-plastic shear modulus (*PREFACT*) was set to 2 a value often used for this type of material. The initial bulk and shear modulus were based on the measured initial Young's modulus. From these assumptions the elastic shear modulus (G) was chosen to be 18.0 GPa and Poisson's ratio 0.18, which gives a bulk modulus of 21.5 GPa and initial Young's modulus of 42.5 GPa. The failure surface parameters A and N were estimated from the experimental data given by FFI in Norway and IC (Imperial College) in the UK, see appendix 2. All other RHT constants are taken from results on similar concrete and can be found in the literature, Riedel (1999, 2000). The values used for the concrete RHT strength model are summarised in table 3.3. For convenience all concrete material constants are also listed in appendix 1 together with a short explanation.

Table 3.3. Material parameters for the RHT concrete model.

Parameter	Values		Parameter	Values
G	18.0 GPa		*Cap on elastic surface*	Yes
f_c	92.0 MPa		B	1.6
f_t/f_c	0.057		M	0.61
f_s/f_c	0.30		α	0.010
A	1.9		δ	0.013
N	0.6		D_1	0.04
Q_2	0.6805		D_2	1
BQ	0.0105		$E_{f,min}$	0.01
PREFACT	2		*SHRATD*	0.13
TENSRAT	0.80		*Tensile failure model*	Hydro tensile limit
COMPRAT	0.75			

For the tensile failure, there are two options that can be used together with the RHT model, and these are "Principal stress" and "Hydro tensile limit". For the principal stress model the user input are "Tensile failure stress", "Maximal shear stress" and "Crack softening". For the hydro tensile limit there is no further input data to be given and this criteria for failure was used for the simulations.

As discussed, a large amount of work is required in order to verify all material data used. However, the parameters describing the failure surface is one of the most important and in figure 3.2 are the experimental failure curves from FFI and IC compared to the curve obtained by using the failure parameters A and N in table 3.3. The stress difference between the compressive load and the confinement pressure equals the deviatoric yield stress. As seen the curves overlap at low pressures, while the calculated curve give a slightly higher stress difference at increasing pressures.

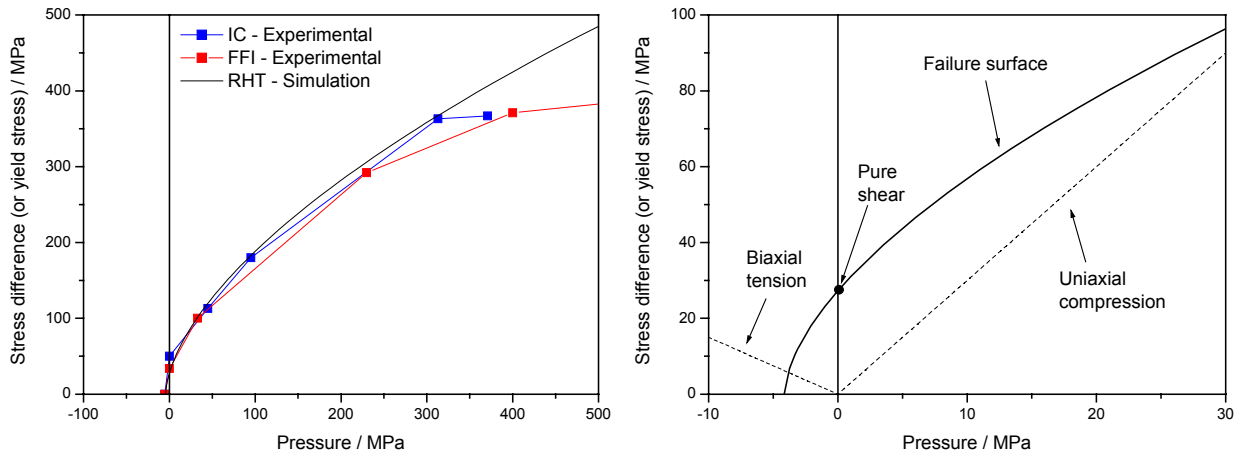

Figure 3.2. The left figure shows the experimental yield stress from FFI and IC compared to the simulated results for a confined steel cylinder. The right part shows an enlarged part of the failure surface. For comparison, the uniaxial compression and the biaxial tension paths are also shown as well as the point representing pure shear load. After Hansson (2001).

The RHT model contains a large number of material parameters and the relative importance of some of the parameters are investigated. As discussed above the values of the RHT constants are determined partly from experimental data and partly estimated from literature data on similar concrete types. Among the parameters with rather large uncertainty are the residual strength (*B, M*), damage evolution ($E_{f,min}$ D_1) and the shear strength (*fs/fc*). Thus, the influence of these material constants on the penetration path are interesting and the tested new values are estimated to be a measure of "a reasonable" uncertainty of the investigated parameters.

The residual strength is a power function of the pressure with the strength constant *B* and strength exponent *M*. Figure 3.3 below shows the effect of changing the residual strength constants to representative values of a concrete with slightly higher residual strength, see also figure 2.1. The area increase is a measure of the increased load bearing capacity in the given pressure range and is 18%. By changing the parameters $E_{f,min}$ and D_1 from their nominal values (0.01 respectively 0.04) to, typical values of a weaker concrete, ($E_{f,min}$ = 0.05 and D_1 = 0.08) the failure strain as a function of pressure is changed according to figure 3.3.

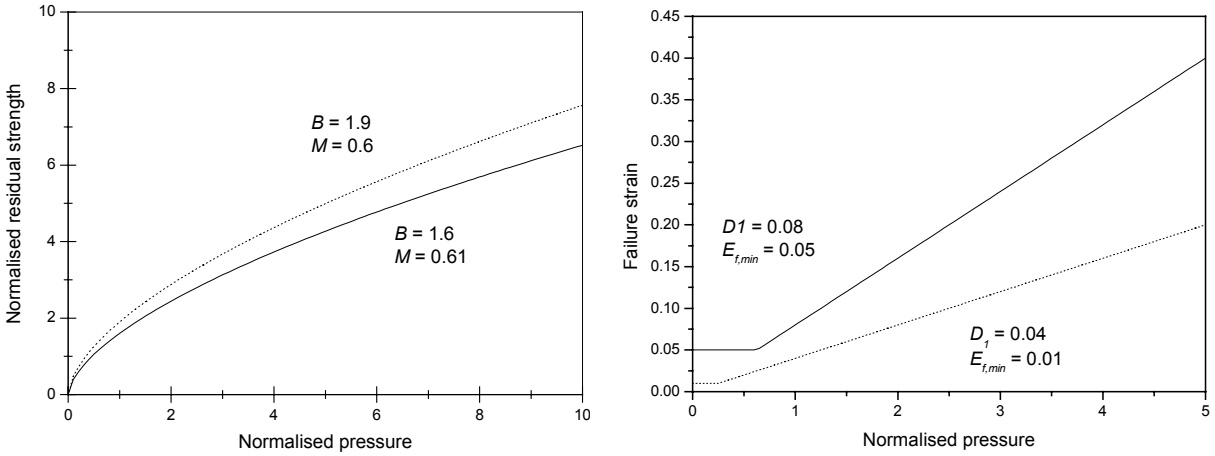

Figure 3.3. Residual strength normalised to the unconfined compression strength f_c =92 MPa (left) and failure strain (right) as a function of pressure normalised to f_c. For the nominal values (solid line) and the new values (dotted line).

The final parameter studied in this investigation is the shear strength. In the RHT model the shear strength is normalised over the compressive strength f_c and is changed from $0.3f_c$ to $0.1f_c$. It is believed that the new value of $0.1f_c$ or 9 MPa, corresponding to a weaker material, gives a better description of the investigated concrete.

The result of the parameter sensitivity study should indicate the relative importance of the material constants and thus determine the experimental effort used to establish the values. In addition, the effects of different processors (Lagrange, ALE, SPH) and geometry considerations with non-normal projectile impact are discussed.

3.2. Problem geometry

The general problem geometry is the same for all simulations and can be studied in figure 3.4 below. The total length of the projectile is 559 mm divided into a cylindrical part and an ogive nose part. The cylindrical part has a length of 324 mm and a radius of 76 mm, while the ogive

nose radius is 380 mm. The element mesh size is about 21.5 mm and 7.4 mm along and across the projectile axis respectively. In the experimental ballistic benchmark test, the inner part of the projectile was instrumented with accelerometers. Thus, in order to get the correct projectile mass for the simulations the inner part of the projectile is modelled with a fictional density seen as the darker inner part of the penetrator in figure 3.4. Since the projectile is not deformed, changing the density has no other effect than giving the correct mass. A Lagrange projectile mesh is used for all simulations, including the 3D calculations

The target is 75 cm thick with a radius of 120 cm divided into 2 circumferential cylindrical subgrids with the outer cylinder enclosing the inner. The inner, central, cylinder has a radius of 50 cm and the outer cylinder covers the remaining part up to the total radius of 120 cm. The inner cylinder has a constant element size of either 10 or 5 mm, while the element size of the enclosing cylinder gradually increases from 10 or 5 mm to 41.1 and 23.6 mm respectively at the limiting radius. This limits the number of elements far away from the impact and thus reduces the computational time considerably with negligible effect on the projectile penetration path. There is no principal difference between the target geometry for the 3D simulations.

3.3. 2D penetration simulations

The numerical simulations of the benchmark test were performed with Autodyn 2D version 4.2.0.3 using both Lagrange and SPH (Smooth Particle Hydrodynamics) element formulation for the concrete target in connection with the advanced RHT material model. Simulation of the benchmark test with Autodyn 4.1.13 and the RHT implemented as a user routine was earlier also done by Svinsås (2001) as well as Hansson (2001) with Autodyn 4.2β.

3.3.1. 2D simulations with Lagrange target formulation

When a Lagrange formulation is used to represent a target during penetration it is necessary to use numerical erosion. However, this causes material to be removed from the mesh and thereby giving reduced mass and confinement. This type of model might give a reasonable result for materials that do not have a pressure dependent yield stress, i.e. steel. However, both concrete and ceramics have a pressure dependent yield stress and failure type, and the calculated results are therefore likely to be influenced by the use of numerical erosion. Despite this, the results can be used to indicate the relative importance of the different parameters. The geometry of the penetration simulations is shown in figure 3.4 below.

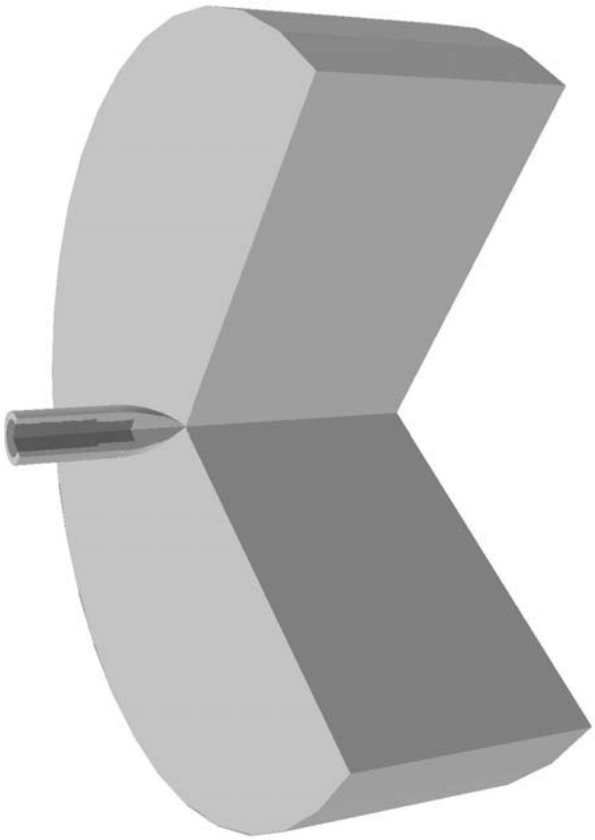

Figure 3.4. Geometry for the 2D-simulations, shown with 270° rotation. The target radius is 1.2 m and the thickness is 0.75 m. The projectile has a total length of 55.9 cm and a diameter of 15.2 cm giving a mass of 46.4 kg. The impact velocity is 459 m/s.

As mentioned earlier, it is necessary to use numerical erosion when a Lagrange formulation is used. Based on previous work by Hansson (2001), using 2D-Lagrange formulations of the target, a numerical erosion value of 150% is used. Hansson reports that higher values of the erosion caused large energy errors due to local contact problems between target and projectile. This phenomenon is likely to origin from the heavily distorted target elements in the contact zone and a typical example is shown in figure 3.5. On the other hand, it was also shown that lower values give a large influence on the calculated projectile exit velocity. Thus, low values on the erosion strain resulted in an increased exit velocity, and high values resulted in an increased energy error for the calculation. Based on the above discussion an erosion strain of 150% was chosen as a reasonable value for the 2D Lagrange simulations performed in this study.

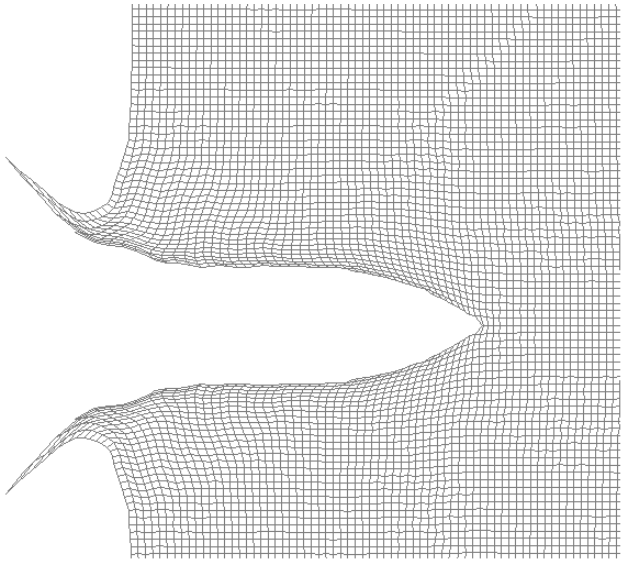

Figure 3.5. Typical figure of the distorted Lagrange target grid during penetration. After Hansson (2001).

In the mentioned previous work the introduction of a friction coefficient of 0.05 between projectile and target did not affect the exit velocity to any significant degree combined with an erosion strain of 150%. However, a significant increase of the energy error was found. The total energy of the problem includes work done, kinetic and thermal energies, and should be constant during the simulation. Therefore, a deviation of the total energy indicates a numerical error and is defined as an energy error. In this case, the increased friction is likely to increase the shear strain in the target, and thereby distort the elements to a larger degree causing increasing numerical difficulties. The friction was therefore neglected for the major part of the Lagrange simulations done in this investigation.

Since the main purpose is to investigate the relative influence of the RHT constants, no complete convergence check of the element size was done and a target cell size of 10 mm was used for the main part of the simulations. Although, in table 3.4 where the calculated exit velocity as a function of element size, erosion and friction is compiled it is seen that 5 mm element size give a somewhat higher exit velocity compared to the case with a mesh using 10 mm cells.

Further discussing the result in table 3.4 the calculations give, in general, a lower exit velocity compared to the results found in the initial work carried out in 2001 by Hansson. However, it must be pointed out that the material parameters have been slightly modified due to more experimental information and no direct comparison of absolute values can be done between the present and the previous investigations. Although the trends found in table 3.4 with increased energy errors if friction is used agrees with the earlier findings. As a final comparison it is noted that the experimentally found exit velocity is close to 190 m/s, or about 10-20 % lower than the numerical results in table 3.4.

Table 3.4. Effect of erosion strain, friction and element size on the exit velocity.

Model identity	B99211	B99212	B99207	B99209
Processor	Lagrange			
Element size (mm)	10		5	
Symmetry	Axial symmetry			
Erosion strain (%)	150	150	150	150
Friction	0	0.05	0	0.05
Energy error (%)	1.5	8.8	0.6	8.8
Exit velocity (m/s)	226	198	237	215

For comparison, the experimental exit velocity was approximately 190 m/s.

Turning to the parameter sensitivity analysis, the influence from the residual strength surface (*B, M*), damage parameters (D_1, $E_{f,min}$) and shear strength (f_s/f_c) on the exit velocity can be found in table 3.5. In this respect, it is important to remember that the scaling of the failure surfaces against the compressive strength will change the residual surface, shear strength and tensile strength for the material model when the compressive strength is varied. This is important to keep in mind when the results from the parameter study are compared with other concrete types. For convenience, the result using the nominal values is included in the right hand column of table 3.5.

Table 3.5. Effect of changes of some material parameters on the exit velocity.

Model identity	B99231	B99219	B99230	B99211
Processor	Lagrange			
Element size (mm)	10			
Symmetry	Axial symmetry			
Erosion strain (%)	150	150	150	150
Friction	0	0	0	0
Material parameter	$D_1 = 0.04$ $E_{f,min} = 0.01$	$fs/fc = 0.1$	$B = 1.9$ $M = 0.6$	Nominal Values
Energy error (%)	1.1	1.0	1.5	1.5
Exit velocity (m/s)	250	222	196	226

For comparison, the experimental exit velocity was approximately 190 m/s.

As seen, changes of the failure strain and the residual strength surface (see also figure 3.3) give a large influence on the calculated exit velocity. On the other hand, the rather large decrease of the shear strength has a minor effect on the exit velocity and the apparent decrease of the velocity is almost within the energy error. The residual strength is increased compared to the nominal values as shown in figure 3.3 and, as a consequence of the stronger target, the exit velocity is decreased with 30 m/s. The area difference between the residual strength curves in figure 3.3 up to a normalised pressure of 10 (or 920 MPa), which approximately is the maximum pressure reached during penetration, corresponds to 18 %. The results show that the residual strength surface is important for penetration calculations and considerable efforts must be taken for its experimental determination.

The change of damage parameters gives failure at a smaller strain and thus a weaker target with a following increase of the exit velocity with 24 m/s. As also seen in figure 3.3 the failure strain is a function of pressure and obviously this is an important parameter which unfortunately also is difficult to determine experimentally.

The residual strength parameters and the damage parameters have a large influence on the calculated penetration path. However, as shown by Hansson (2001) the nominal values used in

the simulations here results in a reasonable size of the damaged concrete surfaces when compared to photos of real post test targets.

As a further comparison between numerical and experimental data, the curves in figure 3.6 show the calculated velocity using the nominal input data (model B99211) and the experimentally found projectile path. As seen the velocity deviation increases with increasing penetration.

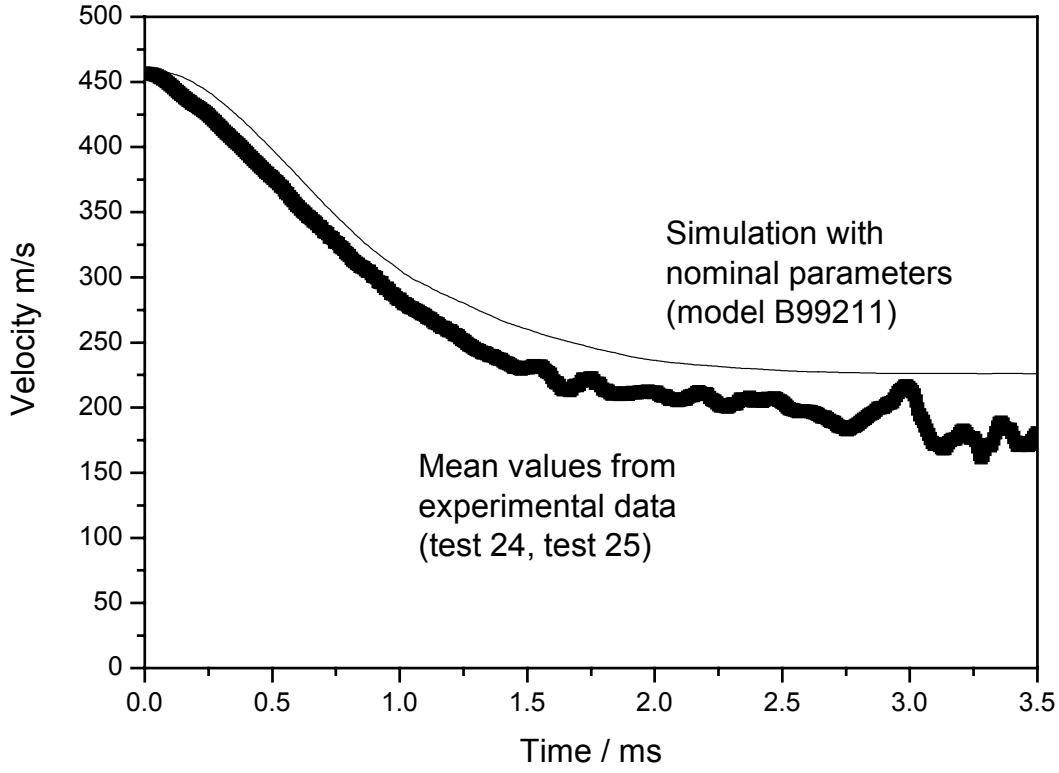

Figure 3.6. Velocity versus time during penetration for a simulation with nominal input data as well as the mean value from experimental data.

The pressure caused by the penetration is important since it affects the various concrete material properties as discussed. The Lagrange simulations uses numerical erosion which deletes heavily distorted elements and thus decreases the confinement pressure and also the mass. The SPH technique discussed below does not use erosion and therefore is a possible improvement.

3.3.2. 2D simulations with SPH target formulation

The Smooth Particle Hydrodynamic (SPH) formulation is in principle a mesh less Lagrangian, where the material is located to nodes instead of elements. Thus, it is not necessary to use numerical erosion for SPH-models. In figure 3.7 a typical SPH target grid is shown. Note that no heavily deformed elements occur in the SPH formulation compared to the Lagrange mesh in figure 3.5.

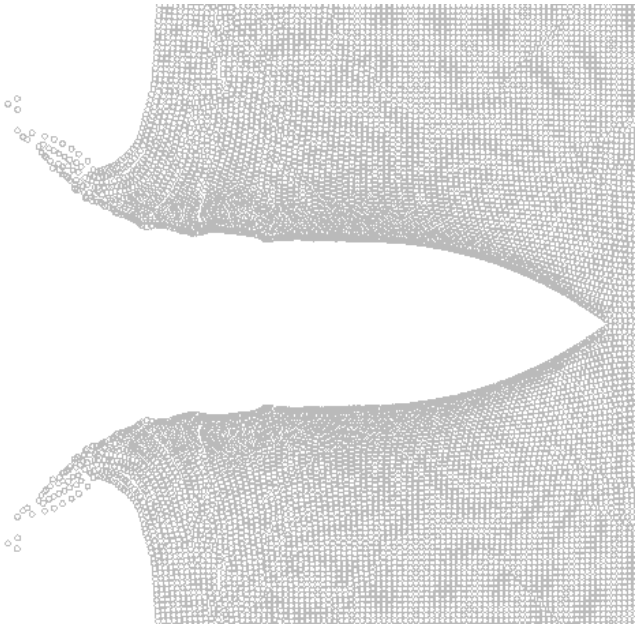

Figure 3.7. Typical target grid using SPH-formulation. As seen, no heavily deformed elements occur. Compare with the deformed Lagrange mesh in figure 3.5. After Hansson 2001.

As in the case with the Lagrange formulation the sensitivity of the exit velocity to changes of the RHT material constants describing the damage evolution (D_1, $E_{f,min}$), residual strength (*B, M*) and the shear strength (*fs/fc*) is investigated. In addition the friction coefficient between the projectile and the target mesh is varied between 0 and 0.1. In table 3.6 and 3.7 the results can be studied.

Table 3.6. Effect of friction and damage parameter on the exit velocity using SPH targets.

Model identity	B99S07	B99S09	B99S11	B99S08	B99S10	B99S12
Processor	Smooth Particle Hydrodynamics (SPH)					
Node size (mm)	5					
Symmetry	Axial symmetry					
Material parameter No erosion	Nominal	Nominal	Nominal	$D_1 = 0.04$ $E_{f,min} = 0.01$	$D_1 = 0.04$ $E_{f,min} = 0.01$	$D_1 = 0.04$ $E_{f,min} = 0.01$
Friction	0	0.05	0.1	0	0.05	0.1
Energy error (%)	0.7	9.2	16.7	0.2	8.9	14.9
Exit velocity (m/s)	215	194	152	243	216	195

For comparison, the experimental exit velocity was approximately 190 m/s.

It is first noted that the SPH formulation with nominal material parameters and no friction gives a lower exit velocity of 215 m/s compared to the corresponding Lagrange case with 5 mm element size (237 m/s). The difference is outside the limit calculated from the energy error and thus, is an effect of the different solution methods. The SPH model may lead to a stronger target, since no erosion is used and as a consequence a lower exit velocity of the projectile. Further, increasing the friction coefficient leads to a decrease in exit velocity as expected, but also to a rapid increase of the energy error. The reason to increased energy errors with the addition of the friction coefficient when using the SPH formulation is not clear.

Turning to the sensitivity test it is noted that weakening the target by starting the damage evolution at a smaller strain give a similar increase in exit velocity as for the Lagrange case. The effect of friction is large but is also accompanied by energy errors.

Table 3.7. Effect of friction and residual strength surface on the exit velocity for SPH targets.

Model identity	B99S13	B99S14	B99S15	B99S16	B99S17	B99S18
Processor	Smooth Particle Hydrodynamics (SPH)					
Element size (mm)	5					
Symmetry	Axial symmetry					
Material parameter No erosion	$B = 1.9$ $M = 0.6$	$B = 1.9$ $M = 0.6$	$B = 1.9$ $M = 0.6$	$fs/fc = 0.1$	$fs/fc = 0.1$	$fs/fc = 0.1$
Friction	0	0.05	0.1	0	0.05	0.1
Energy error (%)	0.9	10.4	18	0.4	9.7	15.8
Exit velocity (m/s)	181	145	99	208	182	151

For comparison, the experimental exit velocity was approximately 190 m/s.

Considering the strength increase of the residual surface as described by B and M we find a decrease of the exit velocity of 34 m/s, the corresponding Lagrange case (with 10 mm element size) gave a decrease of 30 m/s. In addition the effect of friction on the exit velocity is large, but the energy error also increases, when adding a frictional parameter. As seen, changing the residual strength or the damage parameters also gives a clear effect on the exit velocity (181 m/s). On the other hand the large decrease of the shear stress from the nominal value $0.3f_c$ to $0.1f_c$ does not give any marked impact on the exit velocity, see table 3.7.

3.3.3. Conclusions considering 2D simulations

As a summary of the different 2D simulations we find that the RHT parameters residual strength as well as the damage parameters give a large effect on the calculated exit velocities, while the shear stress is of less importance. Thus the experimental effort should focus on determination of the residual strength and damage evolution parameters.

Introducing friction between target and projectile decreases the exit velocity as expected but also gives a rather large increase of the energy error. These conclusions are valid for both Lagrange and SPH formulations of the target. Considering the absolute values of the projectile exit velocities, the SPH model with nominal parameter values (without friction and cell size 5 mm) give a lower exit velocity (215 m/s) than the corresponding Lagrange formulation (237 m/s). For comparison, the experimental figure is 190 ± 10 m/s. Introducing a friction coefficient of 5%, which seems physically reasonable, to the nominal SPH-formulated model gives an exit velocity close to the experimental value. However, both the Lagrange and the SPH calculations result in increasing energy errors if friction is used. The reason for the energy errors using friction in connection with the non-deformed SPH element grid is not known. The errors, of course, give an uncertainty to the calculations. For example, if the calculated exit velocity is 200 m/s and the energy error is 1% this gives a velocity change of 1 m/s if the entire error is attributed to the projectile. Increasing the error to 10% corresponds to a velocity change of 10 m/s at exit. It is finally noted, that the energy error is negative meaning that “energy is lost” and if the lost energy can be tracked to the projectile the projectile speed is underestimated.

3.4. 3D penetration simulations

In this study Autodyn 3D version 4.2.03 is used. The earlier 2D versions of the hydrocode demanded that a symmetry axis were used for the problems. In contrast, 3D simulations are not restricted to any specific symmetry case. This is a major improvement, which allows simulations of more realistic interactions between target and projectile. The major drawback is that the increased number of cells also increases the calculation time.

As in the 2D case a parametric study concerning the effects of different material constants and numerical parameters on the resulting exit velocity for a projectile is done using the 3D version of the software. All material properties for both target and projectile are the same as for the 2D tests and described previously. Apart from material constants, the study includes tests of the importance of erosion strain, friction and element size. The results are compared to previous 2D-simulations and real ballistic tests described earlier. In addition, the 3D version allows different problem geometries to be used, i.e. quarter symmetry and half symmetry cases. Further, in ballistic experiments the projectile often impacts the target at an angle with yaw and pitch and this type of problem can now be simulated using 3D software's which must be considered a major improvement. Thus, a minor study of the effect of different impact angles on the resulting projectile trajectory is done. The majority of the simulations are performed using Lagrange formulated meshes, but some are done with ALE grids as well. As in the 2D cases the target is modelled with 2 circumferential cylinders, see also figure 3.4 and chapter 3.2 where details of the problem geometry are discussed. The inner central cylinder where most of the damage occurs is built up by elements with a constant side length. The outer cylinder surrounding the inner consists of elements where the side length increases with increasing radius, thus decreasing the total number of cells. Despite this, the number of elements in the quarter symmetry models are increased from roughly 10.000 for the 2D simulations to about 180.000 for the 3D meshes with an element side length of 10 mm. Further, the 3D calculations with 5 mm cubic elements consists of 1.200.000 elements. In order to decrease the calculation time for the 3D runs a parallel version of the software is used. The calculation times using 1, 2 and 4 parallel processors are compared and the results discussed.

3.4.1. 3D simulations with Lagrange target formulation

The initial 3D penetration simulations were done using a Lagrange formulation of the target as well as the projectile. As in the 2D case discussed earlier, the initial work is an investigation of the effect of the numerical parameters, erosion strain, element size and friction on the resulting projectile exit velocity. In table 3.8 below the results are tabulated.

Table 3.8. Effects of erosion strain, friction and element size on the exit velocity.

Model identity	B99316	B99311	B99315	B99314	B99312	B99317	B99307	B99309
Processor	Lagrange							
Element size (mm)	10						5	
Symmetry	¼-symmetry							
Erosion strain (%)	100	150	200	100	150	200	150	150
Friction	0	0	0	0.05	0.05	0.05	0	0.05
Energy error (%)	2.4	1.9	1.7	8.1	8.0	7.8	1.9	8.5
Exit velocity (m/s)	234	217	224	214	205	214	225	213

For comparison, the experimental exit velocity was approximately 190 m/s.

As seen, no significant changes of the exit velocity can be found with increasing erosion strain from 100 to 200 % and the projectile speed is close to 220 m/s after penetration. Further, as in the 2D case introducing a friction coefficient largely affects the energy error. It is also seen, that decreasing the cell size to a cube with side length 5 mm instead of 10 mm only give a minor increase of the exit velocity of about 8 m/s.

As a comparison, it is noted that the corresponding 2D-simulations in general give similar values of the exit velocity. It is concluded that an erosion strain of 150 % is sufficient for both 2D and 3D Lagrange simulations. Regarding the element size it seems that both 2D- and 3D-simulations with 5 mm target cells give a slightly higher exit velocity compared to cells with 10 mm side length. In figure 3.8 below the exit velocity is shown as a function of different numerical input data.

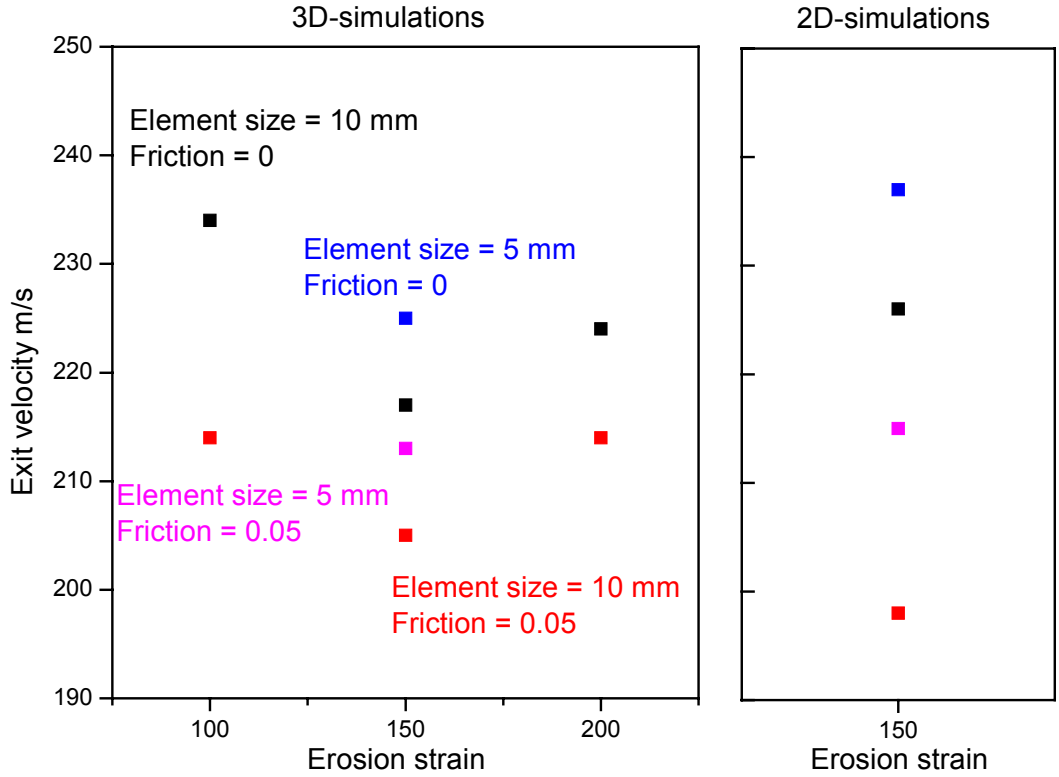

Figure 3.8. Exit velocity as a function of some numerical input data for 2D and 3D simulations.

As discussed before, the RHT model contains a large number of material parameters and the values of the constants are determined partly from experimental data and partly estimated from knowledge of the behaviour of similar concrete types. The parameters describing the transition between the failure and the residual strength surface and the shape of the latter are among the most difficult to assess. Thus, the influence of the residual strength of the crushed material under compression as described by the constants B and M, the parameters ($E_{f,min}$ and D_1) coupled to the degree of damage and also the shear strength (fs/fc) have been investigated. The relative importance of these characteristic parameters are investigated and discussed. In table 3.9 below the resulting exit velocity of the projectile can be studied. Based on previous results, the erosion strain and element size was chosen to 150 % and 10 mm respectively. These parameters as well as the nominal material data and the changes of material data are the same as for the 2D calculations.

Table 3.9. Effect of changes of some material parameters on the exit velocity.

Model identity	B99331	B99319	B99330	B99318	B99311
Processor	Lagrange				
Element size (mm)	10				
Symmetry	¼- symmetry				
Erosion strain (%)	150	150	150	150	150
Friction	0	0	0	0.05	0
Material parameter	$D_1 = 0.04$ $E_{f,min} = 0.01$	$fs/fc = 0.1$	$B = 1.9$ $M = 0.6$	$B = 1.9$ $M = 0.6$	Nominal
Energy error (%)	1.9	1.9	1.9	8.6	1.9
Exit velocity (m/s)	302	243	204	302	217

For comparison, the experimental exit velocity was approximately 190 m/s.

Discussing first the damage evolution it is emphasised that the decrease of the damage parameter from $D_1 = 0.08$ to $D_1 = 0.04$ leads to a larger damage at a given plastic strain, see also equations 12 and 13. Further, the decrease of the minimum strain to fracture leads to earlier failure and thus to a weaker target material. Obviously, the changes give a pronounced softening effect on the target material and the penetration resistance resulting in a marked increase of the exit velocity from 217 to 302 m/s. This is also discussed in connection with the corresponding 2D simulations and the curves in figure 3.3 show the failure strain as a function of pressure for the nominal and the new values of $E_{f,min}$ and D_1. It is however noted that the velocity change is considerably larger in the 3D case compared to the 2D result.

The residual strength is a power function of the pressure with the strength constant B and strength exponent M. Thus increasing B should increase the residual strength, while the decrease in M leads to a lower value of the residual strength. In this case, the over all value of the strength increases and the exit velocity decreases somewhat from 217 m/s to 204 m/s, giving a slightly smaller change than the corresponding 2D calculations, see table 3.5.

The shear strength is normalised over the compressive strength f_c and is decreased from $0.3f_c$ to $0.1f_c$. This decrease of the shear strength of the target leads to less penetration resistance and the projectile speed after penetration is 12% higher i.e. 243 m/s compared to the nominal value.

In figure 3.9 the velocity trajectories for the projectile as it penetrates the target are shown using the different 3D problems in table 3.9 and the corresponding 2D cases in table 3.5.

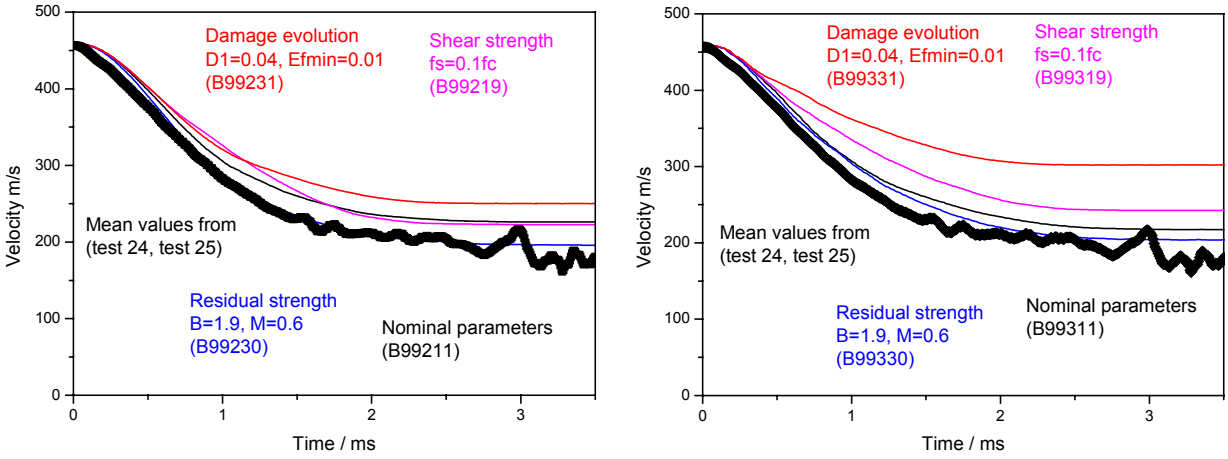

Figure 3.9. Velocity as a function of penetration depth in the target for the 2D (left) and 3D models (right) shown in table 3.5 and 3.9 respectively.

3.4.2. 3D simulations with ALE target formulation

As discussed before, a problem with the Lagrange formulation is that heavily distorted elements may cause numerical problems and must therefore be removed from the mesh and this can affect the solution of the problem studied. The Arbitrary Lagrange Euler (ALE) processor uses also a form of re-meshing of the deformed grid and mapping of the solution to the new grid. Thus, ALE can be seen as an extension of the Lagrange scheme with features of the Euler method where the material is allowed to flow through the mesh. A small number of simulations using the ALE formulation are done and the results are collected and compared to the Lagrange method in table 3.10.

Table 3.10. Effect of changes of processor (ALE or Lagrange) on the exit velocity.

Model identity	B99332	B99333	B99311	B99316
Processor	ALE		Lagrange	
Element size (mm)	10			
Symmetry	¼ -symmetry			
Erosion strain (%)	150	100	150	100
Friction	0	0	0	0
Energy error (%)	1.9	2.4	1.9	2.4
Exit velocity (m/s)	225	234	217	234

For comparison, the experimental exit velocity was approximately 190 m/s.

Obviously the change from a pure Lagrange solver to ALE (Arbitrary Lagrange Euler) does not affect the exit velocity to any significant degree. The Lagrange formulation without friction resulted in an exit velocity of 217 m/s while the corresponding ALE solution gave 225 m/s. The introduction of friction between target and projectile does not alter this conclusion.

3.4.3. 3D simulations with Lagrange target formulation and non-normal impact

The main improvement with the 3D models is the possibility of simulating oblique impact and other cases where no symmetry axes can be used. In this chapter initial work considering different types of impact angles are simulated and the results are discussed and compared with

normal impact calculations. Further, other variations of the geometry (i.e. ½-symmetry) are also compared with the previous ¼-symmetry simulations.

Apart from variations of impact angle where the projectile velocity is parallel with the projectile length axis, the yaw of the projectile can be changed, i.e. the velocity is not parallel with the projectile length axis. The latter case with slight deviations between projectile length axis and the velocity vector is very common in experimental ballistic tests. In table 3.11 the different impact cases are listed together with the results.

Table 3.11. Effect of variations of geometry and impact angles.

Model identity	B99320	B99321	B99322	[a]B99323	B99311	B99312
Processor	Lagrange					
Element size (mm)	10					
Symmetry	½-symmetry				¼-symmetry	
Impact geometry	Normal	Yaw=1°	Yaw=1°	Angle=30°	Normal	Normal
Erosion strain (%)	150	150	150	150	150	150
Friction	0	0	0.05	0	0	0.05
Energy error (%)	1.9	1.9	8.9	2.1	1.9	8
Exit velocity (m/s)	211	186	163	111	217	205

[a]*The impact velocity is 460 m/s parallel with the projectile axis and at an angle of 30° to the surface normal. At exit the centre of mass velocity is 111 m/s moving at an angle of 51° with the normal, see also figure 3.11.*

From table 3.11 some very interesting conclusions can be drawn. It is first noted that at normal impact using ¼ or ½-symmetry results in a similar exit velocity as expected. However, the small deviation of 1° between projectile axis and velocity vector gives a rather large effect on the projectile trajectory and the exit velocity decreases with 25 m/s (12%) to 186 m/s compared to the case with nominal impact. A yaw of one degree is common in ballistic testing and the above results show that the ballistic testing must include measures of projectile yaw and pitch. The graphs in figure 3.10 show the penetration paths with and without yaw (models B99320, B99321).

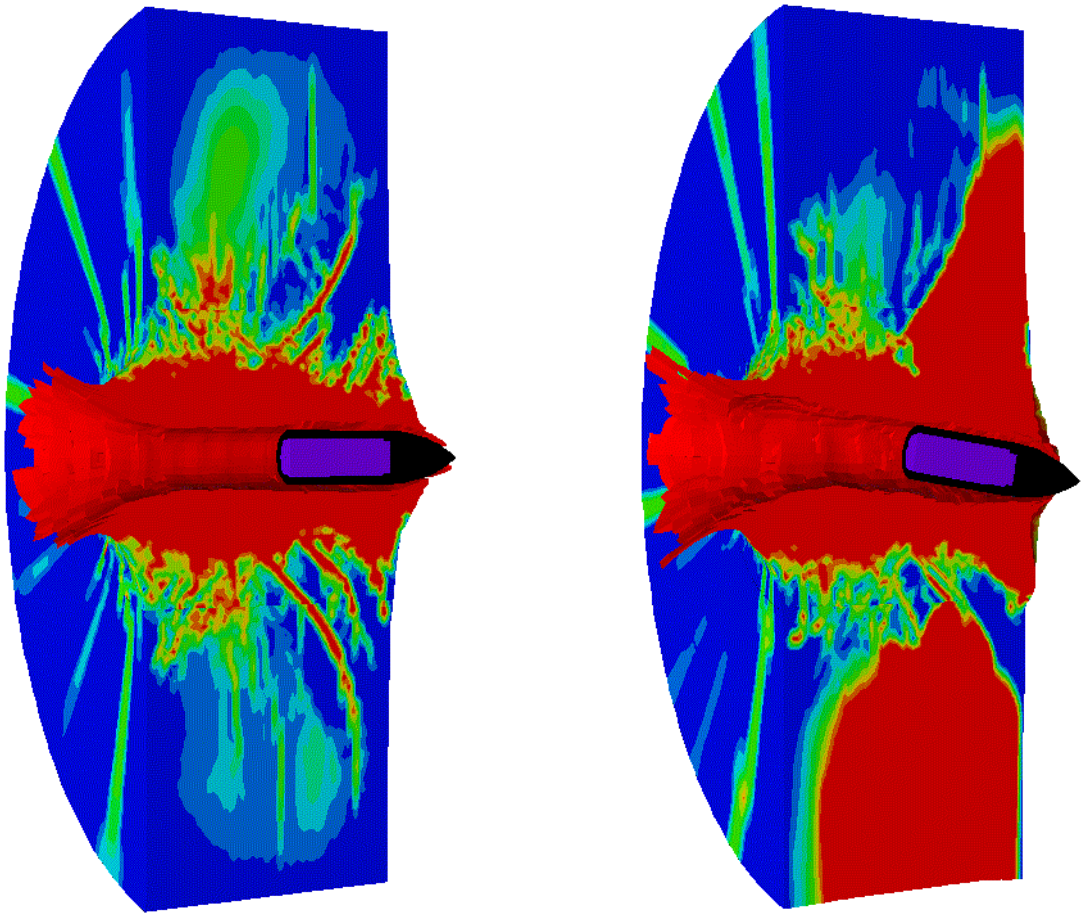

Figure 3.10. Comparison of the penetration path at normal impact (left) and with 1 ° yaw (right).

As seen in figure 3.10 the yaw results in a wider penetration channel and also a curved path through the target. As a consequence more energy is dissipated into the concrete and the exit velocity decreases.

Considering different angles of attack, the graph in figure 3.11 show the projectile trajectory resulting from an impact angle of 30° compared to the normal. The oblique angle causes different pressures on the upper and lower side of the projectile and as a consequence an increasing curvature of the trajectory. At exit, the absolute value of the velocity vector is 111 m/s and the centre of mass moves with an angle of 51°, compared to 30° at impact.

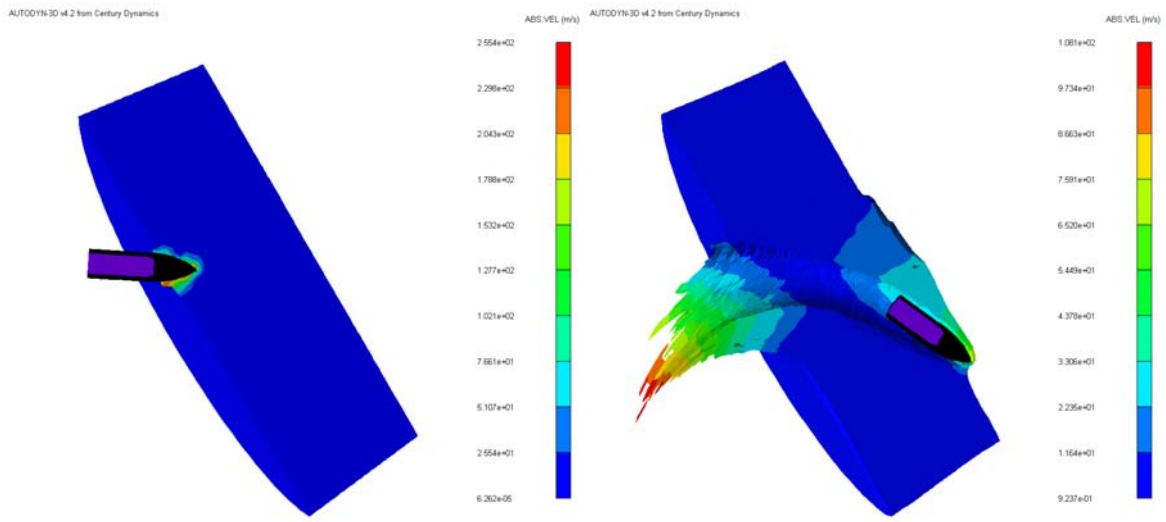

Figure 3.11. Projectile hits the target at a speed of 459 m/s and at an angle of 30°. At exit the absolute value of the velocity is 111 m/s with the centre of mass moving at an angle of 51°.

3.4.4. Conclusions considering 3D simulations

It is clear that the 3D-simulations can give additional and very valuable information considering projectile penetration where the 2D restriction to symmetric cases caused limitations. Perhaps the most important finding is that even a very small yaw of the projectile of 1° results in a large influence on the exit velocity. This type of deviation from normal impact very often occurs at ballistic tests. The simulations show that this must be quantified and taken into account when comparing the performance of projectiles and targets with other experiments and simulations.

Considering the parametric material data study described earlier it is concluded that the 3D simulations with normal impact causes roughly the same results as the 2D simulations. However, it is found that the exit velocity is even more sensitive to the damage parameters using 3D grids, and also the shear stress gives a larger effect than in the corresponding 2D simulations.

3.4.5. Parallel 3D simulations

The introduction of 3D versions of hydrocode softwares is a great enhancement of the possibilities to solve and predict more realistic problems. As a consequence, the use of such softwares is likely to increase rapidly. The obvious disadvantage is that the calculation time increases dramatically due to the increase of the number of elements in the mesh. Therefore, the calculation time using 2 and 4 parallel processors has been compared to the case with a single processor. The test model is labelled B99311, se table 3.11, and the real clock time to calculate problem penetration times of 0.5, 1, 1.5 and 2 ms are measured. The figure below shows the result using 1.7 GHz P4 processors.

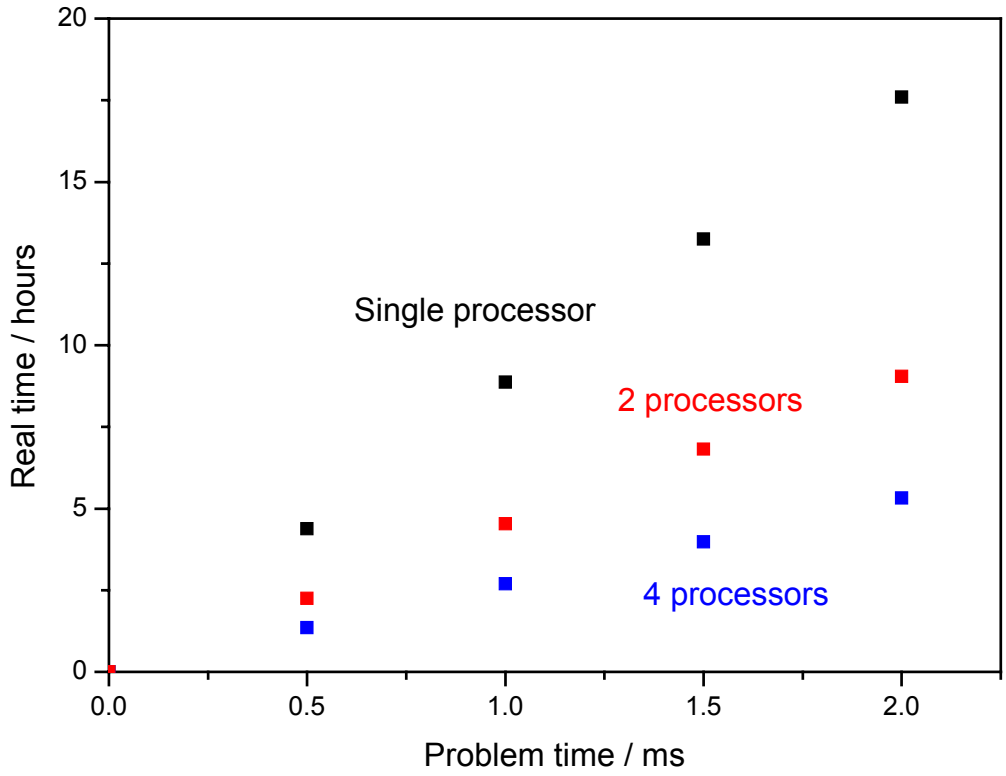

Figure 3.12. Real calculation time versus problem time using a single processor and two or four parallel processor configurations respectively.

From figure 3.12 it is clear that the calculation time decreases substantially using the parallel configuration. With 2 and 4 processors the real computational time is about 1.9 and 3.2 times lower respectively compared to the case with a single processor. These factors depend also on the partitioning of the problem into sub-processes.

In the autumn of 2002 an example of a parallel processing configuration of 4 or 8 processors (P4, 2.53 GHz) with necessary equipment would cost about 60,000 and 115,000 SEK respectively. This processor type is roughly 1.5 times faster compared to the one tested above.

4. DISCUSSION

Considering the material description of concrete, the RHT model is promising. The strength is modelled by three surfaces, representing elastic limit, failure surface or peak load and finally a residual strength of the damaged material under compression. Further, apart from pressure, the strength surfaces are dependent on the strain rate and the triaxial stress state. Thus, this model is able to handle most of the cases that are of importance for projectile penetration into brittle materials like concrete. However, the determination of the material constants require rather extensive experimental work. The parameters describing damage evolution, residual strength and the tensile behaviour are difficult to assess and it is necessary to develop new testing methods to determine damage development in the concrete and strength of damaged or partly damaged concrete.

The numerical methods tested include Lagrange, ALE and SPH. Both the Lagrange and ALE formulations require numerical erosion to obtain a solution. Because of this the mass and confinement in the model decreases during the calculation. This is likely to affect the solution when advanced material models with pressure dependent strength surfaces (as the RHT) are used. The advantage with SPH formulation is that although it in principle is Lagrangian, it is not necessary to use numerical erosion. Preliminary results are very promising and this formulation makes it possible to retain the mass of the target and SPH can also be used to model projectile erosion as well.

The use of the 3D version of the software allows oblique impact, as well as simulations of yaw and pitch angles and must be considered a major enhancement of the possibility to predict the interaction between target and projectile. Unfortunately, there are still software problems using the 3D SPH formulation in connection with the RHT material model that must be solved. One important finding from the Lagrange calculations in this work is that even a very small yaw angle of 1° gives a large effect on the penetration path and exit velocity of the projectile. Thus efforts must be taken to carefully measure the impact geometry of the projectile in future ballistic experiments.

The increase of the calculation time that follows with the rapid increase of elements in the 3D mesh is a problem. However, it is shown that parallel computations using 2 or 4 processors can be used to substantially decrease calculation times.

5. FUTURE RESEARCH

In the near future work should focus on getting good characterised RHT parameters for high performance concrete. Especially damage evolution parameters and residual strength constants are important as shown in this report. However, this involves a large amount of work and must be performed in collaboration with other research institutes. Further, ballistic experiments with measures of not only impact and exit velocities but also of pitch and yaw of the projectile must be conducted. Since it is shown that even very small deviations from normal impact give a large effect on the projectile path through the target. The ballistic experiments should be done in close connection with numerical 3D simulations using preferably the SPH technique. The long term goal is to be able to predict trends in the protective capacity of concrete from mechanical experiments and numerical calculations. To reduce the computational time for the simulations the parallel processor system must be further enhanced.

REFERENCES

AUTODYN Theory Manual. Century Dynamics Ltd. Horsham 2000.

Hansson, H.: Numerical simulation of concrete penetration with Euler and Lagrange formulations, FOI-R--0190--SE, FOI, Tumba 2001.

Hansson, H. and Ågårdh, L.: Experimental and numerical studies of projectile perforation in concrete targets. Proceedings Structural failure and plasticity symposium (IMPLAST 2000), Elsevier, Oxford UK, 2000. pp 115-120.

Herrmann, W.: Constitutive Equation for the Dynamic Compaction of Ductile Porous Materials. Journal of App Physics, Vol 40, No 6, 1969. pp. 2490-2499.

Johnson, G. R., Cook W H: A constitutive model and data for metals subjected to large strains, high strain rates, and high temperatures. Proceedings 7th. International Symposium on Ballistics. Holland, 1983. pp. 541-547.

Meyer, M., A.: Dynamic Behavior of Materials, John Wiley & Sons inc., ISBN 0-471-58262-X, 1994.

Riedel, W.: Ein makroskopische, modulares Betonmodell für Hydrocodes mit Verfestigung, Schädigung, Entfestigung Drei-Invarientenabhängigkeit und Kappe. EMI-Bericht 7/98. EMI Freiburg 1998.

Riedel, W., Thoma K, Hiermaier S, Schmolinske E: Penetration of Reinforced Concrete by BETA-B-500. Numerical Analysis using a New Macroscopic Concrete Model for Hydrocodes. Proceedings of 9th International Symposium on Interaction of the Effects of Munitions with Structures. Berlin, 1999. pp 315 - 322.

Riedel, W.: Beton unter dynamishen lasten, Meso- und makromechanische modelle und ihre parameter. EMI-Bericht 6/00, EMI Freiburg July 2000.

Svinsås, E., O'Carroll, C., Wentzel, C. M. and Carlberg, A.: Benchmark trial designed to provide validation data for modelling. Proceedings of 10th International Symposium on Interaction of the Effects of Munitions with Structures. San Diego, May 2001.

Willam, K. J., Warnke, E. P.: Constitutive Model for the Triaxial Behaviour of Concrete. Seminar on Concrete Structure Subjected to Triaxial Stresses. IABSE Proc. 19, Italy, 1975.

Ågårdh, L. and Hansson, H.: Perforation of steel fibre reinforced concrete slabs with fragments in the velocity range of 1400 – 1600 m/s. Workshop proceedings from Material test procedures in support of dynamic material modelling. FOA-R--99-01227-311--SE. FOA, Tumba, November 1999.

Ågårdh, L. and Hansson, H.: Perforation of steel fibre reinforced concrete slabs with steel fragments in the velocity range of 1400 – 1600 m/s – Trials and simulations.
FOA-R--99-01143-311--SE. FOA, Tumba, April 1999. (In Swedish)

APPENDIX 1: EQUATIONS AND PARAMETERS

Table A.1.1. General parameters and their relationships.

Parameter	Definition / Relationship
Sound velocity	c
Mass	m
Volume	v
Stress	σ
Density	$\rho = m/v$
Initial density	$\rho_0 = m/v_0$
Strain rate	$\dot{\varepsilon} = \varepsilon/t$
Bulk modulus	$K = \rho \cdot c^2 = \frac{E}{3(1-2\nu)}$
Poisons ratio	$\nu = \frac{E}{2G} - 1$
Young's modulus	$E = \sigma/\varepsilon = 3K(1-2\nu) = 2G(1+\nu)$
Shear modulus	$G = \frac{E}{2(1+\nu)}$
Compression	$\mu = \frac{\rho}{\rho_0} - 1$
Linear EOS	$P = \mu \cdot K$
Polynomial EOS	$P = A_1\mu + A_2\mu^2 + A_3\mu^3$

Table A.1.2. Equation of state parameters for the concrete target.

P-alpha equation of state		
Parameter	**Explanation**	**Nominal value**
ρ_0	Initial density	2.39 g/cm^3
ρ_{porous}	Porous density	2.39 g/cm^3
C_{porous}	Porous sound speed	3000 m/s
p_{crush}	Initial compaction pressure	80 MPa
p_{lock}	Solid compaction pressure	1800 MPa
N	Compaction exponent n	5
Solid EOS	Type of solid EOS, i.e. Polynomial	
ρ_{solid}	Reference density for solid EOS	2.54 g/cm^3
A_1	Parameter A_1 for polynomial EOS, for compression.	40 GPa
A_2	Parameter A_2 for polynomial EOS, for compression.	0 GPa
A_3	Parameter A_3 for polynomial EOS, for compression.	0 GPa
B_0	Parameter B_1 for polynomial EOS	1.22
B_1	Parameter B_2 for polynomial EOS	1.22
T_1	Parameter T_1 for polynomial EOS, for expansion.	40 GPa
T_2	Parameter T_2 for polynomial EOS, for expansion.	0 GPa
T_{ref}	Reference temperature	300 K
C_v	Specific heat	640 J/kgK

Table A.1.3. RHT strength parameters for the concrete target.

RHT strength model		
Parameter	**Explanation**	**Nominal value**
G	Shear modulus	18 GPa
f_c	Compressive strength	92 MPa
f_t/f_c	Tensile compressive strength ratio	0.057
f_s/f_c	Shear compressive strength ratio	0.30
A	Failure surface parameter A, initial slope of failure surface	1.9
N	Failure surface exponent N, pressure dependence for failure surface	0.6
Q_2	Tensile compression meridian ratio	0.6805
BQ	Brittle to ductile transition	0.0105
$\frac{G_{elastic}}{G_{elastic-plastic}}$	Ratio between elastic shear modulus and elastic-plastic shear modulus. (PREFACT)	2
$f_{t,\,elastic}/f_t$	Ratio between elastic surface and failure surface for tension (TENSRAT)	0.8
$f_{c,\,elastic}/f_c$	Ratio between elastic surface and failure surface for compression (COMPRAT)	0.75
Cap option	Use cap on elastic surface	Yes
B	Residual strength constant, initial slope of residual surface	1.6
M	Residual strength exponent, pressure dependence for residual surface	0.61
α	Compressive strain rate exponent	0.01
δ	Tensile strain rate exponent,	0.013
D_1	Damage constant	0.08
D_2	Damage exponent	1
$\varepsilon_{fail,\,min}$	Minimum strain to failure	0.05
$G_{residual}/G_{elastic}$	Residual shear modulus fraction (SHRATD)	0.13
Tensile failure model	Use of "Hydro tensile limit" or "Principal stress" for tensile failure description	Hydro tensile limit
P_{min}	Hydro tensile limit failure	Yes
$\sigma_{tensile\ failure}$	Tensile failure stress for "Principal stress" failure condition	Not used
$\tau_{maximum}$	Shear failure stress for "Principal stress" failure condition	Not used
Gf	Crack softening for "Principal stress" failure condition	Not used

APPENDIX 2: BENCHMARK TESTS

In October 1999 a series of benchmark tests were conducted at the Bofors test centre. These tests were a cooperation project with DERA, FOA, FFI and TNO as participants. The purpose with the benchmark tests was to obtain reliable data for numerical simulations, and be able to test the available numerical methods and material models for simulation of penetration in concrete. This appendix describing the mechanical and ballistic testing is from chapter 3 in the report by Hansson (2001) but are for convenience and clarity also included in this report.

Material properties

The concrete for the benchmark test series was tested with standard methods to obtain the E-modulus, cube strength and splitting strength. The behaviour of the concrete during tri-axial loading were tested, using passive confinement of the concrete with GREAC cells, by FFI in Norway and Imperial College in the UK. The properties of the concrete targets are given in tables A.2.1 to A.2.3 and in figures A.2.1 to A.2.4.

Table A.2.1. Properties of the concrete targets.

Target/concrete properties	**Value**
Diameter	2.40 m
Length	0.75 m
Compressive uni-axial cube strength*	103 ± 2 MPa
Compressive uni-axial cylinder strength**	92 ± 2 MPa
Tensile splitting strength*	6.5 ± 0.2 MPa
Tensile splitting strength**	5.9 ± 0.6 MPa
Initial E-modulus** (E_0)	44.0 ± 0.5 GPa
E_c **	44.5 ± 0.9 GPa

*Note: *: Determined on cubes with 150 mm side.*
***: Determined on ∅100×200 mm cylinders.*

Table A.2.2. Specimen of concrete tested in GREAC cell by FFI.

Test no.	Steel cylinder				Weight of specimen (gram)	Initial length (mm)	Initial density (g/cm^3)	Date of testing
	O.D (mm)	I.D (mm)	Length (mm)	Material				
X	122	76.4	150	Hardened Orvar Supreme	1624	148.1	2.39	9/11/99
IX	101.6	76.2	150	High strength steel NS 13411-05	1624	148.7	2.39	15/10/99

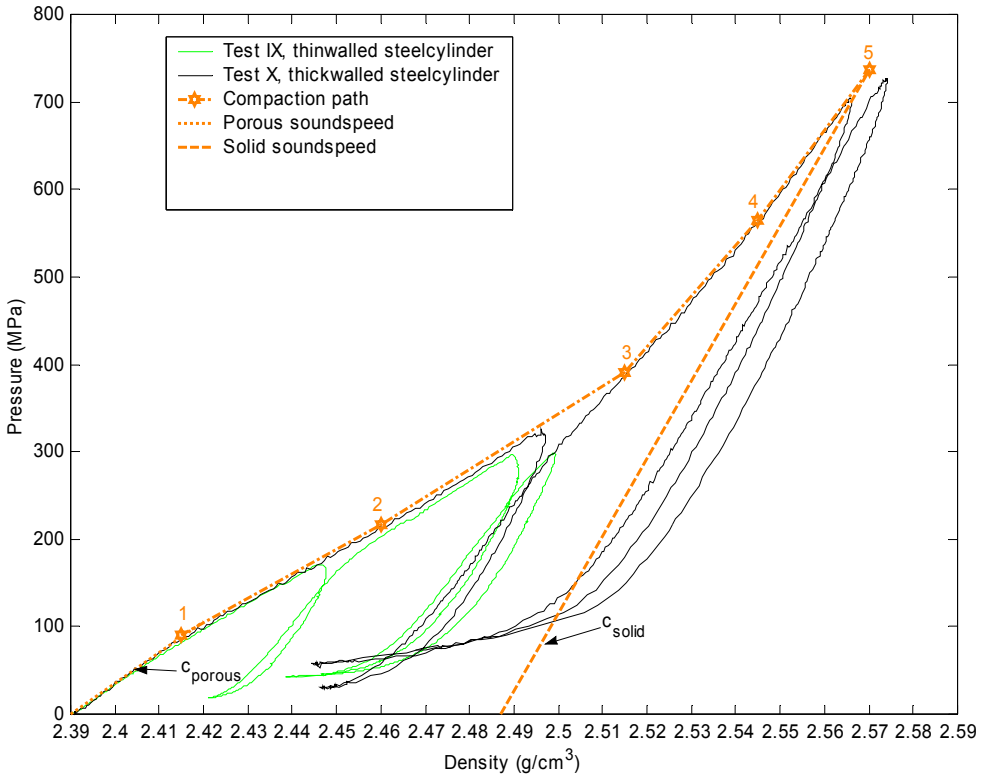

Figure A.2.1. Pressure vs. density for samples tested at FFI.

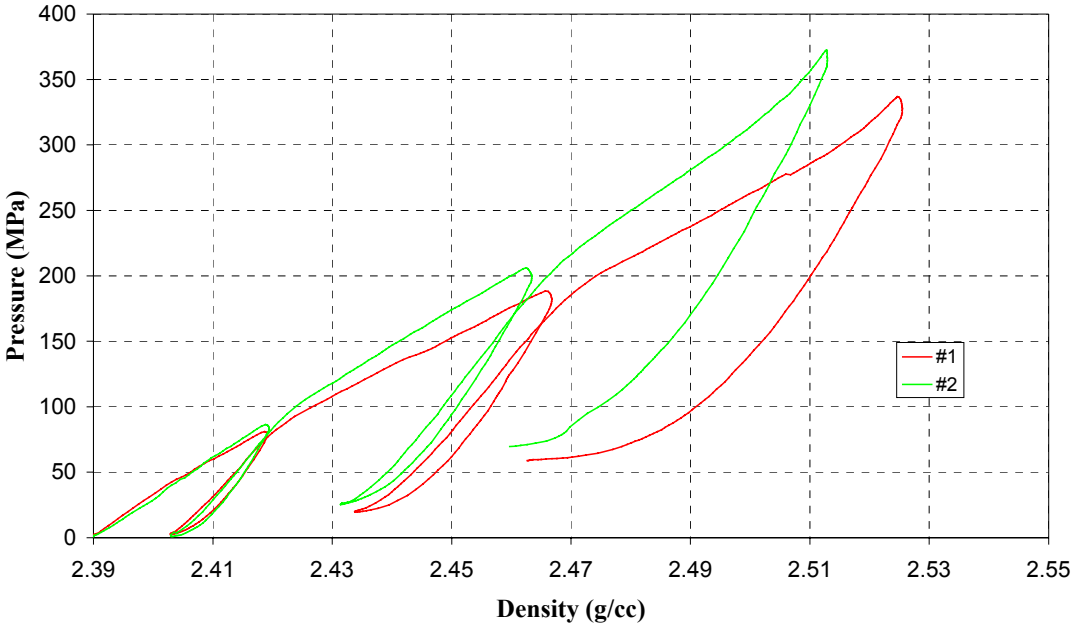

Figure A.2.2. Pressure vs. density for samples tested at Imperial college.

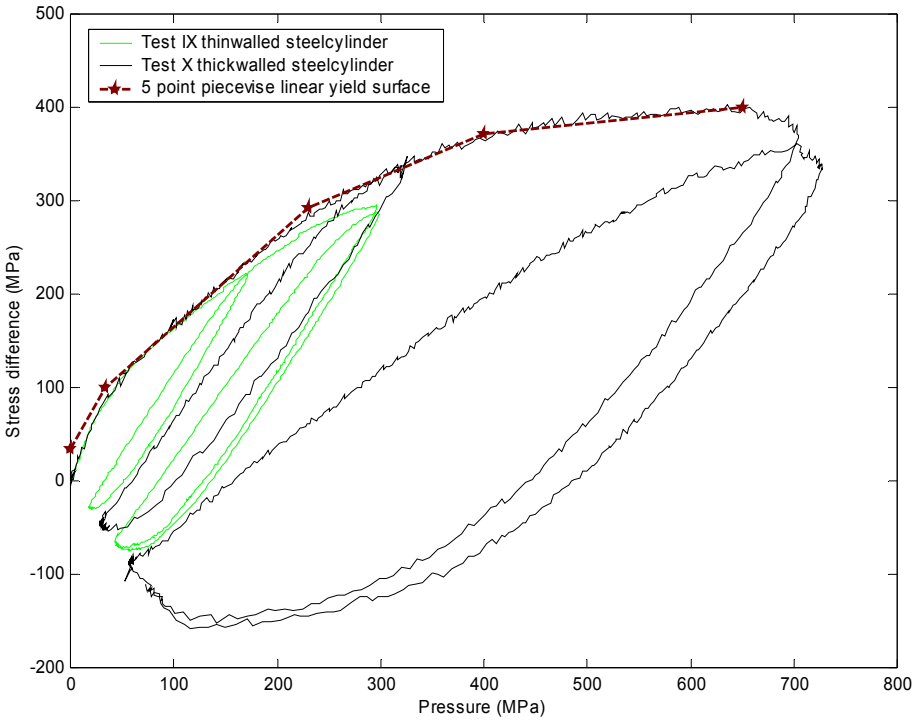

Figure A.2.3. Stress difference vs. pressure for samples tested at FFI.

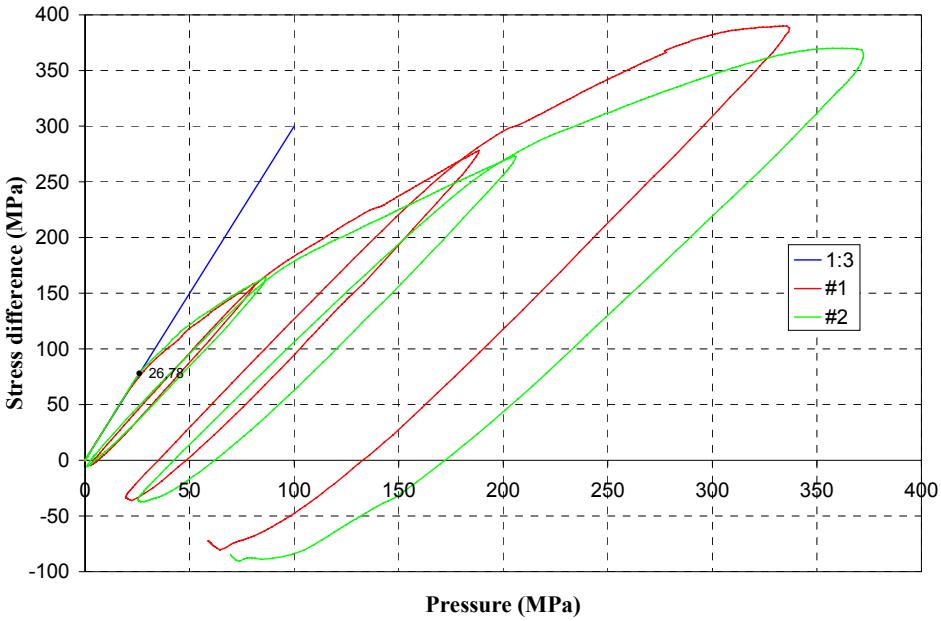

Figure A.2.4. Stress difference vs. pressure for samples tested at Imperial College.

Table A.2.3. Compiled concrete data from tests performed at FFI.

Porous sound velocity		Solid sound velocity	
$c_p = \sqrt{\frac{dp}{d\rho}} = \sqrt{\frac{105 \cdot 10^6 \, N/m^2}{2420 - 2390 \, Kg/m^3}} = 1871$ m/s		$c_s = \sqrt{\frac{dp}{d\rho}} = \sqrt{\frac{737 \cdot 10^6 \, N/m^2}{2570 - 2487 \, Kg/m^3}} = 2980$ m/s	
5 point piecewise linear compaction path			
	Density (g/cm^3)	Pressure (MPa)	
1	2.415	90	
2	2.460	216	
3	2.515	390	
4	2.545	565	
5	2.570	737	
5 point piecewise linear yield surface			
	Pressure (MPa)	Stress difference (MPa)	Hardening slope
1	0	34	
2	33	100	2.00
3	230	292	0.97
4	400	371	0.46
5	650	400	0.12
Shear modulus			
$G = \frac{1}{2}\frac{ds}{de} = 10417$ MPa			
Porous bulk modulus		Solid bulk modulus	
$K_p = \frac{p}{\varepsilon_V} = \frac{88}{0.01} = 8800$ MPa		$K_p = \frac{p}{\varepsilon_V} = \frac{750}{0.072 - 0.042} = 25000$ MPa	

Benchmark penetration tests

The benchmark penetration tests were performed with an instrumented spinning projectile with 152 mm diameter, see figure A.2.5 and A.2.6 and table A.2.4. Three tests were conducted with unreinforced concrete with the approximate cube strength of 100 MPa. Two of the projectiles were equipped with accelerometers to determine the deceleration during the perforation in the target. The exit velocity of the projectiles was determined with a high speed video camera for comparison with data from accelerometer recordings and Doppler radar measurements. Two of the targets were equipped with pressure transducers, which were mounted 30 cm from the back face of the targets. The impact and exit velocities of the projectiles are given in table A.2.4. A target before impact is shown in figure A.2.7, and the targets after perforation are shown in figures A.2.8 to A.2.10

Numerical integration of the accelerometer signal from instrument pack in the projectile underestimated the velocity of the projectile in comparison with velocity measurement from Doppler radar and exit velocity determined by high speed video. The radar measurements seem to have registered the velocity during the major part of the projectile deceleration in the target. Also the lower projectile exit velocity for test 25 in comparison with test 24 is shown in the radar measurements. The data from accelerometers, radar and pressure transducers are shown in figures A.2.11 to A.2.17.

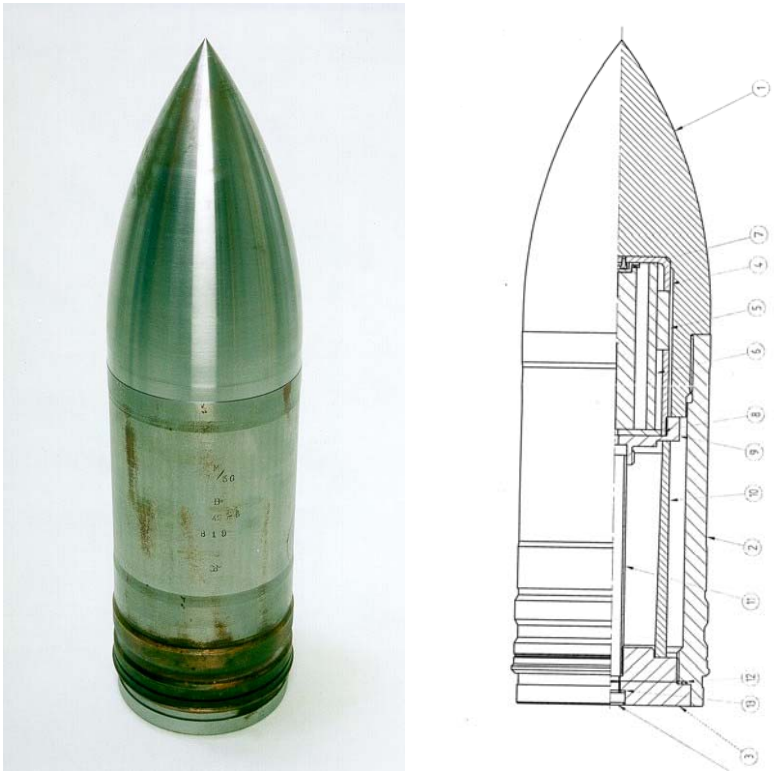

Figure A.2.5. Projectile for benchmark tests.

Figure A.2.6. Dummy projectile after test 23.

Table A.2.4. Benchmark test data.

	Test 23	**Test 24**	**Test 25**	**Mean value**
Diameter	152 mm			
Length	552 mm			
Ogive radius	380 mm			
Nose length	228 mm			
Total mass	46.2 ±0.1 kg			
Mass of case	38.8 kg			
Type of projectile	Dummy	Instrumented*	Instrumented	----
Impact velocity	460.0 ±0.5 m/s	455.5 ±0.2 m/s	458.8 ±0.2 m/s	458.1 ±0.2 m/s
Exit velocity**	183 ±6 m/s	204 ±4 m/s	181 ±4 m/s	190 ±14 m/s

**: Instrumentation pack not recovered after test.*
***: Determined from high speed video.*

Figure A.2.7. Target mounting.

Figure A.2.8. Target after perforation for test no. 23, front face to the left.

Figure A.2.9. Target after perforation for test no. 24, front face to the left.

Figure A.2.10. Target after perforation for test no. 25, front face to the left.

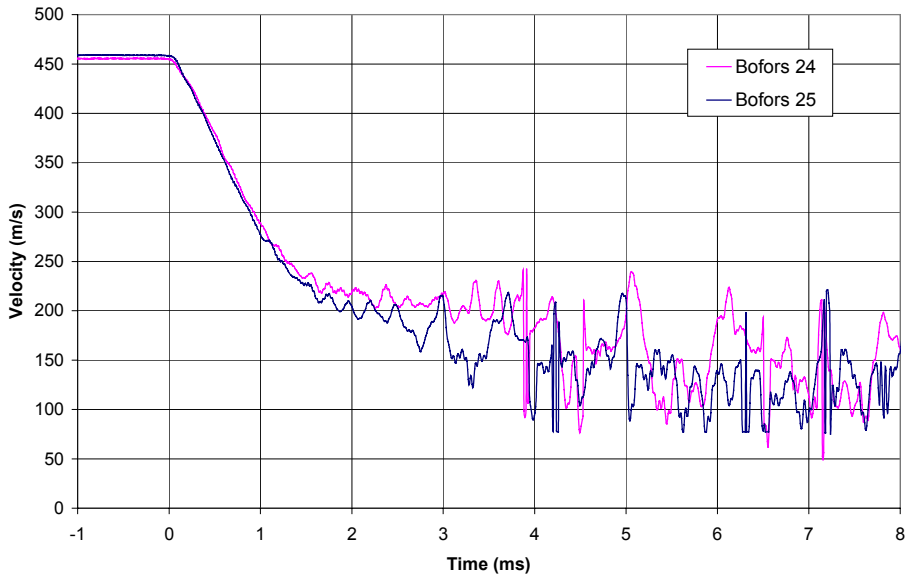

Figure A.2.11. Doppler radar measurements of velocity for the instrumented projectiles.

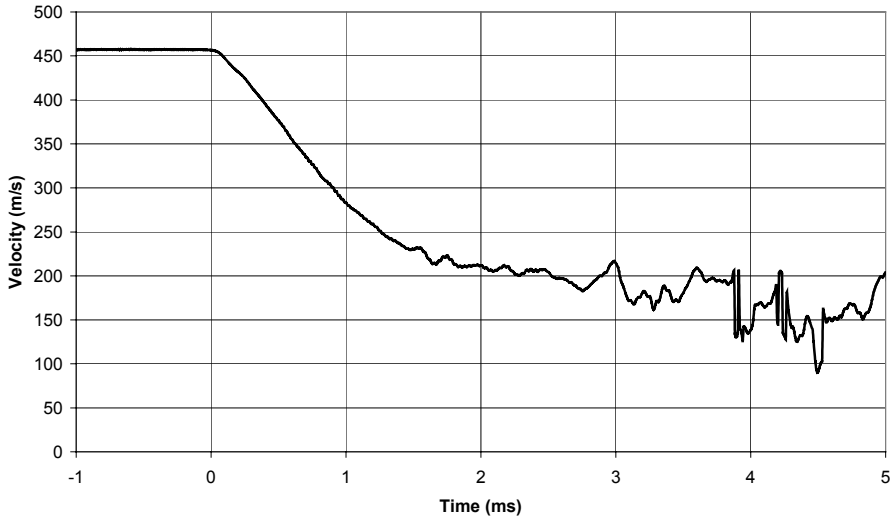

Figure A.2.12. Mean values of radar measurements for tests 24 and 25.

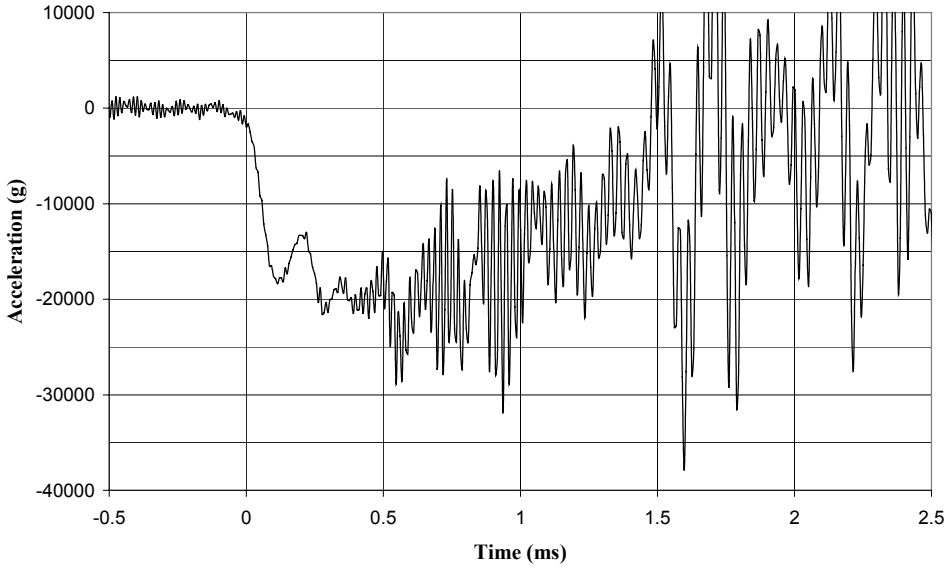

Figure A.2.13. Calculated deceleration of projectile based on mean velocity values from radar measurements for tests 24 and 25.

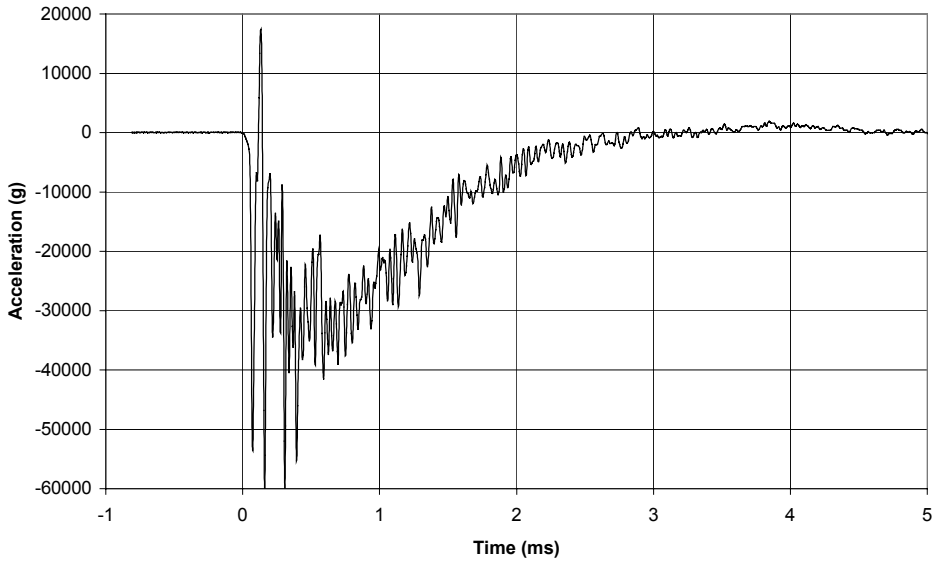

Figure A.2.14. Acceleration registration from projectile for test no. 25.

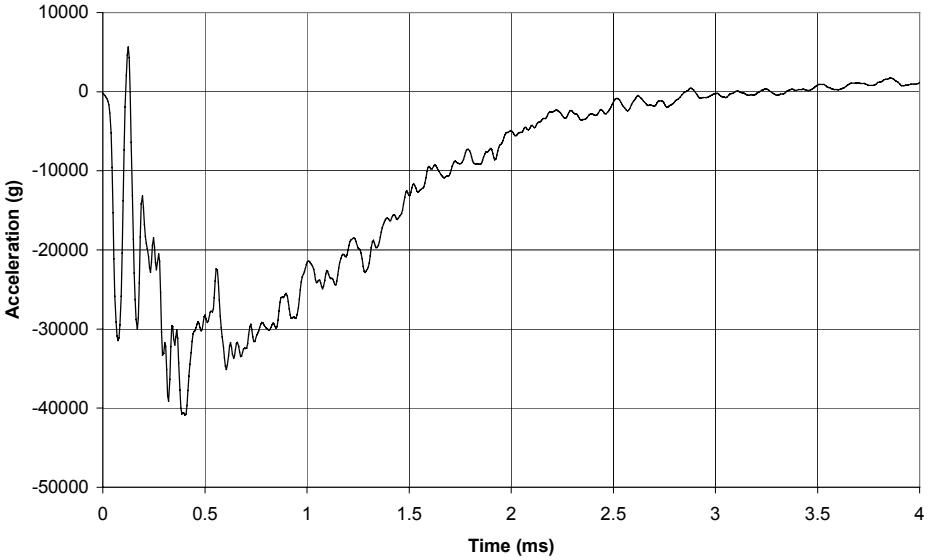

Figure A.2.15. Moving average of 9 points for acceleration registration from projectile for test no. 25.

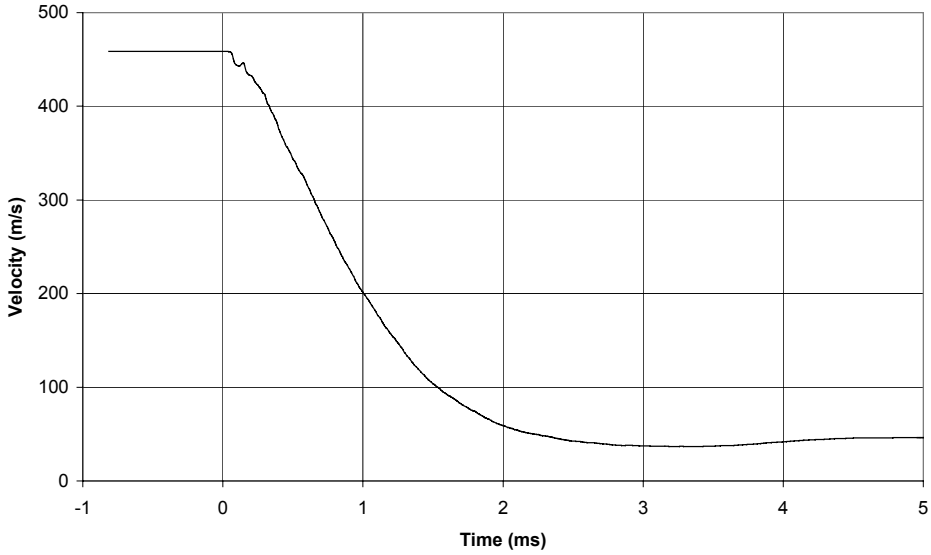

Figure A.2.16. Velocity of projectile obtained by integration of acceleration data from projectile for test no. 25.

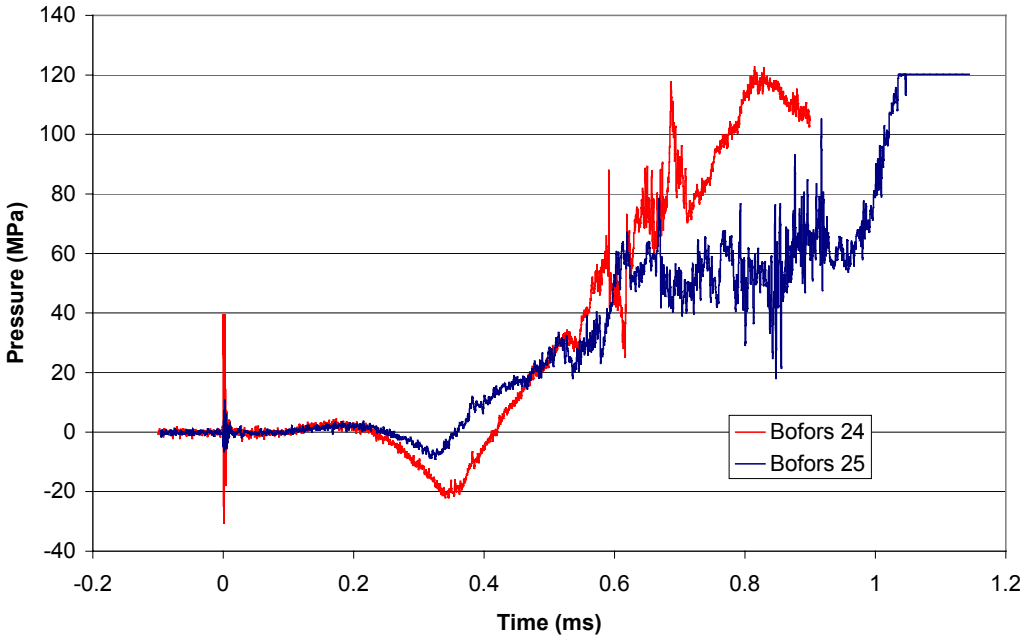

Figure A.2.17. Measured pressure in the concrete targets for test no. 24 and 25.